Formation of the axial relief at the very slow spreading Southwest Indian Ridge (49° to 69°E)

Mathilde Cannat, Celine Rommevaux-Jestin, Daniel Sauter, Christine Deplus, Véronique Mendel

JOURNAL OF GEOPHYSICAL RESEARCH, VOL. 104, NO. B10, PAGES 22,825–22,843, OCTOBER 10, 1999

Formation of the axial relief at the very slow spreading Southwest Indian Ridge (49° to 69°E)

Mathilde Cannat,[1] Céline Rommevaux-Jestin,[1] Daniel Sauter,[2] Christine Deplus[3] and Véronique Mendel[2,4]

Abstract. The comparison of segment lengths, relief, and gravity signature along the very slow spreading Southwest Indian Ridge (SWIR) between 49°E and 69°E suggests that the marked change in segmentation style that occurs across the Melville transform (60°45'E) reflects a change in the modes of formation of the axial topography. We propose that the axial relief east of Melville is largely due to volcanic constructions that load the axial lithosphere from above. By contrast, the axial relief in segments west of the Melville fracture zone appears to be primarily due, as proposed for segments of the faster spreading Mid-Atlantic Ridge, to along-axis changes in the depth of the axial valley, and to partial compensation of negative loads (thicker lower crust and/or lighter upper mantle) acting within the plate, or at the bottom of the plate. In terms of geology, this means that the contribution of the uppermost, effusive, part of the crust to along-axis crustal thickness variations may be greater east of Melville than in other regions of the study area. Regional axial depths suggest that the ridge east of Melville is also characterized by a low melt supply and is underlain by cold mantle. A simple model of mantle melting and regional isostatic compensation suggests that differences in mantle temperature and in melt thickness between this deep eastern ridge region, and the shallower region west of the Gallieni transform (52°20'E), are of the order of 80°C and 4 km, respectively.

1. Introduction

The morphology of mid-ocean ridges is affected in systematic ways by changes in spreading rate: fast spreading ridges (full rates of 80 mm/yr or more) have an axial high, while slow spreading ridges (full rates of 40 mm/yr or less) generally have an axial valley [*Macdonald*, 1982]. Slow-spreading ridges also display more pronounced along-axis variations of axial depths and crustal structure than faster spreading ridges. Systematic studies of along-axis variations in axial topography [*Fox et al.*, 1991; *Grindlay et al.*, 1992; *Sempéré et al.*, 1993], gravity signature [*Kuo and Forsyth*, 1988; *Lin et al.*, 1990; *Rommevaux et al.*, 1994; *Gente et al.*, 1995; *Detrick et al.*, 1995], and seismic velocity structure [*Purdy and Detrick*, 1986; *Tolstoy et al.*, 1993; *Wolfe et al.*, 1995] at the Mid-Atlantic Ridge (MAR) have led to the definition of a typical segment of this slow spreading ridge (full rate 24 to 40 mm/yr). The center of the segment is shallower, with a narrow to locally nonexistent axial valley, a mantle Bouguer anomaly (MBA) low, and Moho depths of 6 to 9 km. Segments ends are marked by a wider and deeper axial valley, gravity highs, and a shallower Moho. Segments are 20 to 100 km long, and are generally limited by transform or nontransform offsets. Because crustal thickness variations are probably mainly due to along-axis variations of the magma supply, the segmentation of the MAR axis suggests that magma is not evenly distributed along-axis but focused toward the center of each segment [*Kuo and Forsyth*, 1988; *Lin et al*, 1990]. The focusing mechanism has been proposed to be active mantle upwelling beneath segments centers [*Whitehead et al.*, 1984; *Lin et al.*, 1990] but remains a matter of debate [e.g., *Magde et al.*, 1997].

Axial depths at a slow spreading ridge result from two distinct mechanisms: the partial isostatic compensation of loads emplaced on top, within, and under the axial lithosphere (volcanic constructions, variations in the thickness of middle and lower crustal layers, changes in the density of the upper mantle beneath the ridge), and the extensional deformation of this axial lithosphere leading to the formation of a dynamically supported axial valley. An intriguing characteristic of the MAR is that, although the general presence of a deep and wide axial valley suggests that the axial lithosphere is strong [*Tapponnier and Francheteau*, 1978; *Phipps Morgan et al.*, 1987; *Lin and Parmentier*, 1989; *Chen and Morgan*, 1990], the correlation of along-axis bathymetry and gravity variations is good, suggests near Airy compensation of the along-axis relief, and is therefore consistent with the axial lithosphere being weak [*Blackman and Forsyth*, 1991; *Neumann and Forsyth*, 1993]. This apparent contradiction has been refered to by Neumann and Forsyth [1993] as the "paradox of the axial profile". The explanation they proposed for this paradox is that extensional deformation and the formation of the axial valley contribute a significant part of the MAR axial relief. The depth of this axial valley being controlled by the ridge's thermal regime is correlated with magma supply and mantle

[1]Centre National de la Recherche Scientifique UPRESA 7058, Laboratoire de Pétrologie., Université Pierre et Marie Curie, Paris
[2]Centre National de la Recherche Scientifique UMR J0533, Institut de Physique du Globe, Strasbourg, France.
[3]Centre National de la Recherche Scientifique UMR 7577, Laboratoire de Gravimétrie, Institut de Physique du Globe, Paris.
[4]Now at Challenger Division for Seafloor Processes, Southampton Oceanography Center, Southampton, England, United Kingdom.

Paper number 1999JB900195.
0148-0227/99/1999JB900195$09.00

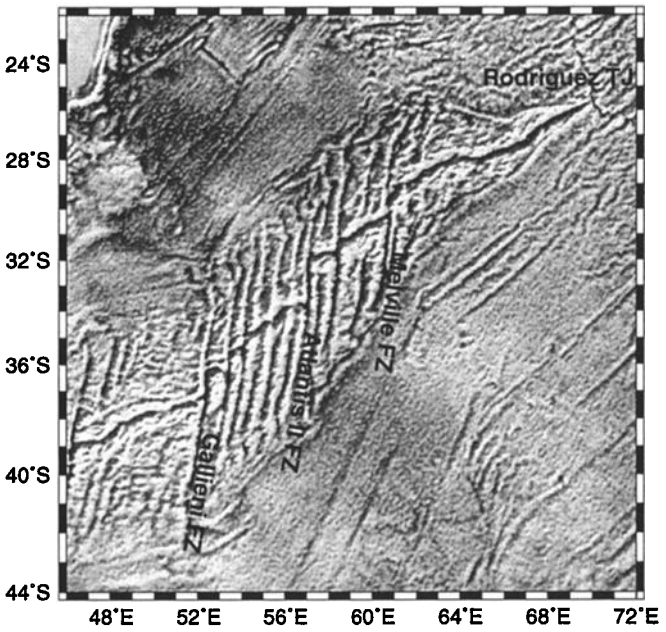

Figure 1. Shaded map of free air gravity anomalies derived from satellite altimetry [*Sandwell and Smith*, 1997]. Note the prominent off-axis traces of axial discontinuities between the Gallieni and Melville fracture zones and the absence of a similar pattern to the east and to the west.

temperature, hence with the gravity signature of the ridge axis. Numerical models of axial valley formation as a function of the ridge's thermal regime successfully reproduce the range of axial depth variations observed along the MAR and are therefore consistent with this hypothesis [*Phipps Morgan et al.*, 1987; *Lin and Parmentier*, 1989; *Chen and Morgan*, 1990; *Neumann and Forsyth*, 1993; *Shaw and Lin*, 1996].

Our understanding of how slow spreading ridges work is to this date mostly based on studies of the MAR. The Southwest Indian Ridge (SWIR) has an even slower spreading rate (full rate 1.6 cm/yr [*DeMets et al.*, 1990]) and has recently been mapped along a significant portion of its length [*Munschy and Schlich*, 1990; *Mendel et al.*, 1997; *Patriat et al.*, 1996; *Grindlay et al.*, 1998]. In this paper, we analyze the axial relief and its gravity signature in the area comprised between 49°E (west of the Gallieni fracture zone) and 69°E (about 100 km to the west of the Rodriguez triple Junction; Figure 1). We use the bathymetry and gravity criteria developed in along-axis studies of the MAR to define axial segments, measure their along-axis relief and gravity signature, and use these data to propose that large volcanic edifices play a significant role in the formation of the SWIR axial relief. A passive upwelling, decompression mantle melting model is then used to estimate the range of large-scale along-axis variations in upper mantle temperature and magma production in the study area, assuming that axial depths, averaged over long portions of the ridge, reflect isostatic balance. We use these estimates in a discussion of what processes control the formation of the axial relief in different regions of the SWIR and of what this could imply for the geology of the crust in these regions.

2. General Setting of the Study Area

Bathymetry (Figure 2) and gravity data over the SWIR axis between 49° and 70°E have been acquired during three cruises: the Rodriguez cruise (RV *Jean Charcot*, 1984 [*Munschy and Schlich*, 1990]), the Capsing cruise (RV *L'Atalante*, 1993 [*Patriat et al.*, 1997]), and the Gallieni cruise (RV *L'Atalante*, 1995 [*Patriat et al.*, 1996]). Acquisition and processing of these data are described by *Munschy and Schlich* [1990], *Mendel et al.* [1997], and *Rommevaux-Jestin et al.* [1997]. The MBA was derived from merged shipboard free air anomaly (FAA) data from the three cruises, by subtracting the effect of the topography and of a Moho assumed to follow the topography with a constant 5 km crustal thickness [*Rommevaux-Jestin et al.*, 1997].

Spreading rate (1.6 cm/yr) and spreading direction (NS) are constant in the study area [*DeMets et al.*, 1990]. The SWIR has been propagating eastward at the Indian Ocean Triple Junction, and accretion ages therefore increase from east to west from about 5 Myr (A3) at 69°E, to about 64 Myr (A29) at 49°E [*Patriat and Segoufin*, 1988; *Sauter et al.*, 1997]. Other obvious variables in the spreading environment of different parts of the study area are the obliquity of the ridge axis (with respect to the normal to the spreading direction), and the presence or absence of long-lived transform and nontransform discontinuities. This last parameter is readily assessed from the satellite-derived FAA map (Figure 1)[*Sandwell and Smith*, 1997]): - the ridge portion west of the Gallieni fracture zone (49°E to 52°20'E) has an overall obliquity of 15° and is devoid of long-lived transform and nontransform discontinuities; - the ridge portion between the Gallieni and Melville fracture zones (52°20'E to 60°45'E) has an overall obliquity of 40° and comprises many long-lived transform and nontransform discontinuities; - and the ridge portion east of the Melville fracture zone (60°45'E to 69°E) has an overall obliquity of 25° and is devoid of long-lived transform and nontransform discontinuities.

3. Along-Axis Bathymetry and Gravity Variations

Drawing a linear axis at a slow spreading ridge supposes that the plate boundary is, at least on a short timescale, linear, while the existence of an axial valley suggests instead that plate separation is accommodated within a zone of deformable lithosphere [*Tapponnier and Francheteau*, 1978; *Phipps Morgan et al.*, 1987; *Lin and Parmentier*, 1989]. For the purpose of comparing along-axis bathymetry and gravity variations, however, we have drawn a linear axis, using conventions explained in Figure 3. This linear axis (Figure 2) represents the probable location of the most recent volcanic activity (neovolcanic ridge or center of the axial magnetic block) or the center of the axial deformation zone (deepest point of the axial valley). It differs only marginally from that used in previous along-axis studies of the area [*Rommevaux-Jestin et al.*, 1997; *Mendel et al.*, 1997] and is interrupted in three small regions (near 53°E, 62°30'E, and 65°E; Figure 2) because of incomplete axial bathymetry coverage. A fourth gap at 66°20'E corresponds to the overlap of two valleys, separated by a broad east-west trending ridge, 1500 m high [*Mendel et al.*, 1997]. We have preferred to leave this 40-km-long region out of our study because the nature of this broad ridge is uncertain: it exposes gabbroic rocks in its lower slopes [*Mével et al.*, 1997], it appears to be underlain by thin crust and therefore to be dynamically supported [*Rommevaux-Jestin et al.*, 1997], but it has a clear normal polarity magnetic signature [*Patriat et al.*, 1997] . We have also left the ridge portion between 69°E and the Rodriguez Triple Junction at

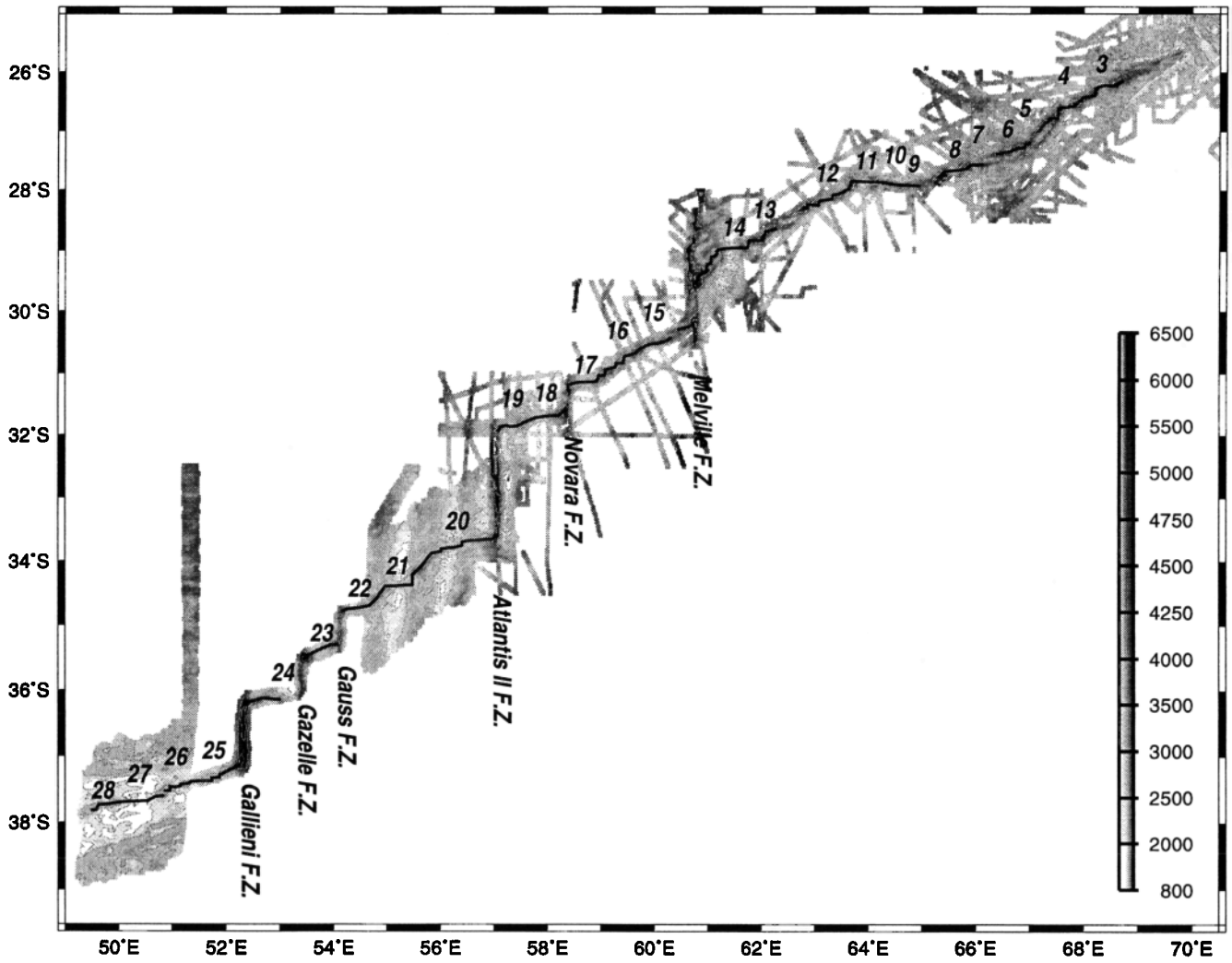

Figure 2. Southwest Indian Ridge bathymetry between 49°E and the Rodriguez Triple Junction (see text for references) with location of ridge segments 3 to 28. Black lines, ridge axis.

70°E out because its gravity signature is strongly influenced by the hotter thermal regime of the nearby Central and Southern Indian Ridges [*Rommevaux-Jestin et al.*, 1997].

3.1. Along-Axis Bathymetry Variations

Mean axial depths (obtained by averaging the axial depth profile in each region) decrease eastward from 3090 m west of the Gallieni fracture zone, to 4230 m between the Gallieni and Atlantis II fracture zones, 4430 m between the Atlantis II and Melville fracture zones, and 4730 m east of the Melville fracture zone (Figure 4). This large-scale variation of axial depths suggests that the regional density structure of the axial region also varies, the ridge east of Melville being underlain by, on average, thinner crust, and/or denser mantle, than the ridge west of Gallieni. A broad positive anomaly of *S* waves velocities, also consistent with a colder and thus denser mantle, is observed in the eastern part of the study area [*Debayle and Lévêque*, 1997].

Short-wavelength variations of axial depths (Figure 4) have led us to define 26 segments (numbered 3 to 28, segments 1 and 2 being closer to the Rodriguez Triple Junction outside the study area; Figure 2). These segments are bounded by transform faults or by nontransform and zero offset discontinuities. The boundary between two adjacent segments is defined as the deepest point in these discontinuities. Nontransform discontinuities and zero offset discontinuities

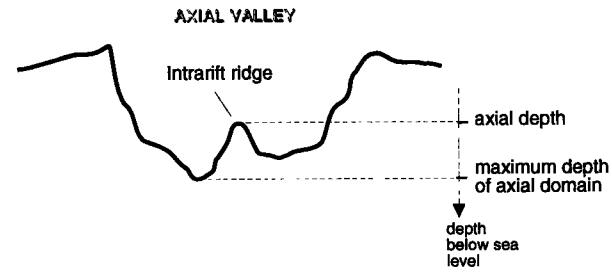

Figure 3. Schematic profile of the axial valley. The axis drawn in Figure 2 is defined as the top of the intrarift ridge, interpreted as a neovolcanic feature. In places where this intrarift ridge is absent, the axis is defined as the deepest point of the axial valley, and in the absence of an axial valley, as the center of the axial block of positive magnetization. Along-axis variations of axial depth and of the maximum depth of the axial domain are shown in Figure 4a.

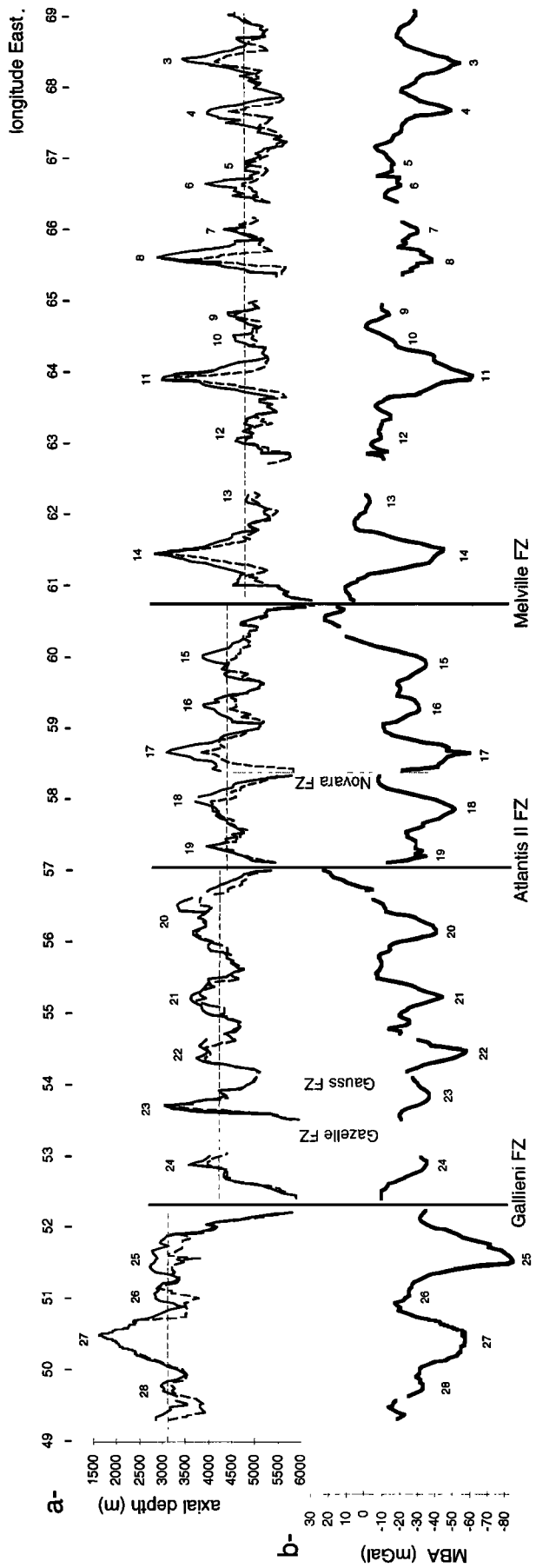

Figure 4. (a) Bathymetry and (b) mantle Bouguer gravity anomaly (MBA) profiles along the axis of the SWIR between 49°E and 69°E. Each ridge segment is numbered as in Figure 2. Axial depth (solid lines) and maximum depth of the axial domain (dotted lines) as defined in Figure 3. Horizontal dashed lines show average axial depth in the west of Gallieni, Gallieni to Atlantis II, Atlantis II to Melville and east of Melville regions.

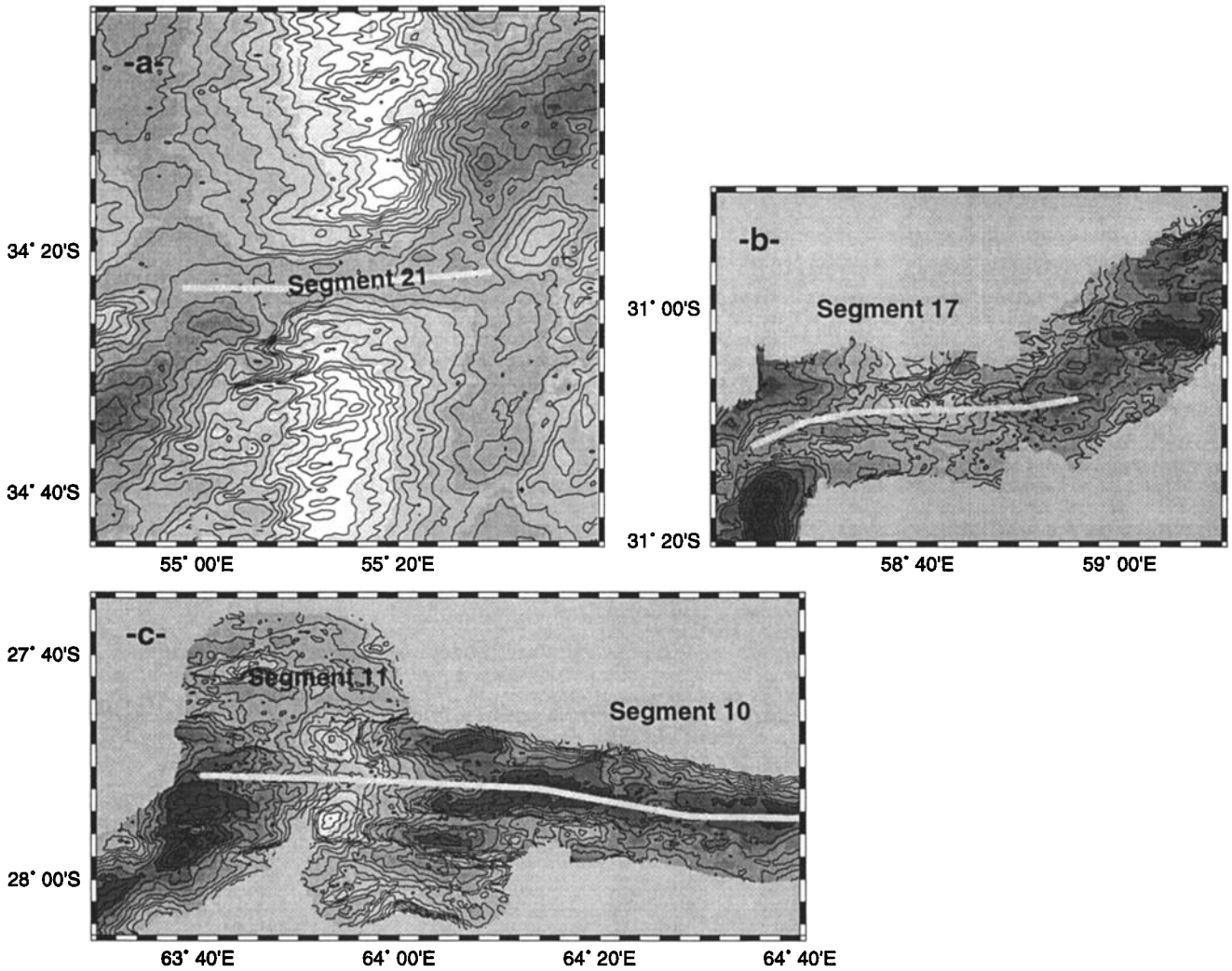

Figure 5. Bathymetry of ridge segments 21, 17, and 10 and 11. Same scale, contour interval 200 m. Dark grey, depths greater than 5000 m; white, depths shallower than 2000 m. Solid grey lines show the location of the center part of each segment. (a) Segment 21, (b) segment 17, and (c) segments 10 and 11. Segments 10 and 11 are separated by a deep basin that does not correspond to an offset of the ridge axis. See Figure 4 for corresponding along-axis bathymetry and gravity profiles.

differ from those in the Atlantic [*Mendel et al.*, 1997; *Rommevaux-Jestin et al.*, 1997] in that they are generally longer in the along-axis direction. As an example, the nontransform discontinuity between segments 20 and 21 (Figure 4) is 110 km long, for an offset of 67 km. Nontransform discontinuities therefore make up significant portions of the along-axis length of many segments. In plan view (Figures 5a and 5b), a segment bounded by nontransform discontinuities is typically composed of a central, more elevated part that trends nearly east-west (perpendicular to the spreading direction), and of two deeper and more oblique (up to 45° in segments 16 and 21) distal parts. The overall trend of the segments varies between N55° (segment 21) and N96° (segment 10) and is generally of the order of N65 to N75° (Table 1).

It is worth noting at this point that there is no unique way to define ridge segments. *Mendel et al.* [1997], for example, have chosen to restrict their segments to the portions of the ridge axis that trend perpendicular to plate motion: that is, to the central portions of the segments defined here. We have preferred to include the oblique portions of the axis (i.e., the wide nontransform discontinuities) in our definition, in order to work on a continuous axial profile similar to that taken into account in comparable along-axis studies of the Mid-Atlantic Ridge [*Lin et al.*, 1990; *Detrick et al.*, 1995; *Thibaud et al.*, 1998]. The definition chosen by *Mendel et al.* [1997] is, however, probably more consistent with the original definition of ridge segments as portions of the ridge limited by axial discontinuities [*Macdonald et al.*, 1988; *Grindlay et al.*, 1991; *Sempéré et al.*, 1993].

Figure 4 also shows along-axis variations of the maximum depth of the axial domain, which differs from axial depths by the height of the intra rift ridge (Figure 3). A coincidence or a near coincidence of the two depths in Figure 4 indicates either that there is no volcanic ridge, or only a very small one, in the axial valley inner floor (this is commonly the case at segments ends), or that there is no axial valley, or a very narrow and shallow one (this is the case at the center of segments 11, 14,

Table 1. Length, Trend, Longitude at Western Extremity, Relief, and Along-Axis Variation of Mantle Bouguer Gravity Anomalies (ΔMBA) for Bathymetric and Gravimetric Segments 3 to 28

	Bathymetric Segments					Gravimetric Segments			
Segment	Longitude E	Length, km	Trend, N	Relief, m		Longitude E	Length, km	Trend, N	ΔMBA, mGal
3	68.60	44 0	67.6	1833	(1437)	68.71	84 5	64.1	-35.8
4	67.87	38 9	67.6	1536	(1302)	67.95	101.7	53 8	-34.4
5	67.00	26.0	61.0	319		66.98	26.6	67.9	-6.5
6	66.78	42.6	74.6	1304	(898)	66.73	33.2	70 0	-12.2
7	66.12	26.2	86.8	851		66.12	28.3	78 4	-9.1
8	65.86	59.2	67.4	2581	(1914)	65.73	44.3/81	70.4	-24.2
9	64.95	26 4	93 1	574		64.95	26.4	93 1	-6.4
10	64 68	45.4	96.3	555	(327)				
11	64.23	60 4	79 3	2672		64.68	104.7	86 6	-53 1
12	63 63	92.3	67.0	1185					
14	61 77	65.1	66 0	2352		61.86	73 8	68 9	-40.4
15	60 32	73.6	67.0	1287	(920)	60.32	73.6	67 0	-31.1
16	59 62	71.6	57.1	1330	(975)	59 48	52 1	48 0	-16.4
17	58.99	63.2	64 4	2376	(1993)	58.95	54.6	76.2	-38.4
18	58.35	79.3	73.8	1840	(1676)	58.23	66.4	77 8	-35
19	57.55	47.5	70.9	1299		57.55	47.5	70.9	-14.6
20	57.02	145.3	66.2	1327		57.02	116 0	71 7	-42 1
21	55.59	88.9	54.8	1114		55.49	54.5	59.8	-32.9
22	54.80	61.5	69.8	934		54 80	61.5	69.8	-36.1
23	54.10	63.3	66.5	1150		54.10	63.3	66.5	-13
25	52.25	91.4	69.9	1300	(1068)	52.25	91.4	69.9	-51.3
26	51.28	41.5	71.0	668	(475)				
27	50.85	85.1	76.1	1895		50 85	85 1	76.1	-30.6
28	49.91	39.1	72.3	630	(504)	49.91	39.1	72.3	-10.7

Relief values between parentheses have been measured on an axial bathymetric profile that averages the axial depth and the maximum depth of the axial domain (as defined in Figure 3) Bathymetric segments 10, 12, and 26 do not have a gravity signature (see Figure 4)

and 27). Axial ridges are particularly prominent in the center of some segments, resulting in significant differences between the two depths (in segments 3, 4, 6, 8, 10, 15, 16, 17, 18, 20, 25, 26, and 28). The values listed between parentheses next to segment relief in Table 1 are reliefs calculated for an axial bathymetry profile that averages these two depths.

The length of most segments varies (Table 1) between 26 km (segment 5) and 92 km (segment 12). Segment 20 is exceptionally long (145 km). Its highest point (56°30'E; Figure 2) , however, is aligned with a north-south trending off-axis bathymetry low and gravity high that we interpreted as the trace of a small offset nontransform discontinuity. The volcanic ridge that goes down from there into the Atlantis II nodal basin appears to have recently propagated westward into the discontinuity. The present-day length of segment 20 therefore reflects a recent change in the local segmentation pattern, probably related to the persistent lengthening of the Atlantis II transform over the past 10 Myr [*Dick et al.*, 1991].

Along-axis reliefs (Figure 6) vary between 319 m (segment 5) and 2672 m (segment 11). The topographic high in segment 23 has an even greater relief (2848 m) but is offset to the west of the local MBA minimum and located near the intersection with the Gazelle transform (Figure 4). We interpret this high as a tectonic feature (northern slope of the inside corner high associated to the Gazelle transform), not a volcanic ridge. The along-axis relief measured from the top of the less elevated volcanic ridge that does coincide with the MBA minimum for this segment (Figure 4) is of only 1150 m (Table 1).

As previously shown by *Mendel et al.* [1997], the segmentation pattern varies markedly across the Melville fracture zone (Figure 4). West of Melville, and particularly between the Gallieni and Melville fracture zones, along-axis bathymetry variations look like those at the MAR, with relatively homogeneous segment lengths and along-axis relief (Figure 4). By contrast, segment length and relief east of the Melville fracture zone are highly variable: six segments

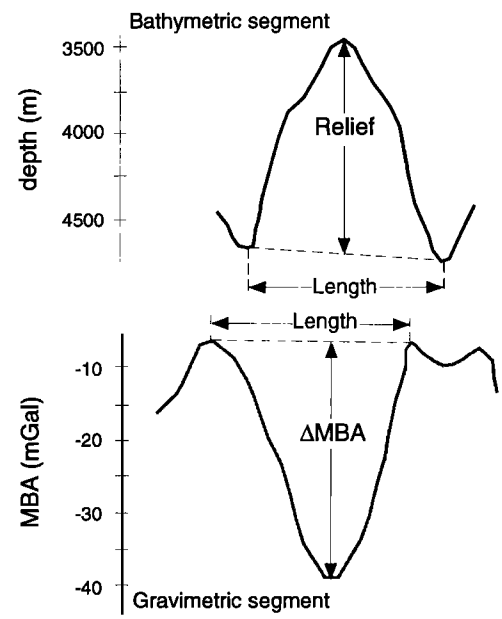

Figure 6. Schematic along-axis bathymetry and mantle Bouguer gravity anomaly (MBA) profiles defining (top) the length and relief of a bathymetric segment, and (bottom) the length and ΔMBA of a gravimetric segment (values listed in Table 1).

(segments 5, 7, 9, 10, 12, and 13; 26 to 92 km in length) have reliefs smaller than 1185 m; three segments (segments 3, 4, and 6; 39 to 44 km in length) have reliefs between 1304 and 1833 m (similar to the highest relief MAR segments); and three segments (segments 8, 11, and 14; 59 to 65 km in length) have reliefs between 2352 and 2674 m. These three very high relief segments are distant from one another by 190 km or more, the intervening segments (9, 10, and 12, 13; Figure 2) having much smaller reliefs (Figure 4).

3.2. Short Wavelength Along-Axis Gravity Variations

Short-wavelength variations in axial MBA also display the change in style associated with the Melville fracture zone, segments to the east of this fracture zone having a less regular pattern of MBA variations (Figure 4) [*Rommevaux-Jestin et al.*, 1997]. In a typical MAR segment, the segment's ends correspond to topographic lows and to MBA highs and the segment's center corresponds to a topographic high and a MBA low [*Lin et al.*, 1990]. In our study area, and particularly to the east of the Melville fracture zone, portions of the axis that are limited by two consecutive MBA maxima do not in every case coincide with the segment defined on the bathymetry (Figure 4). We will use the terms "gravimetric segments" or "gravimetric segmentation" for ridge portions limited by two consecutive MBA maxima (Figure 6). The length, trend, and amplitude (ΔMBA) of gravimetric segments in the study area are listed in Table 1. Segments 10, 12, and 26 are 41 to 92 km long, have reliefs of 554 to 1185 m, but do not correspond to a gravimetric segmentation. Gravimetric segment 3, 4, 11, and 14 are longer than corresponding bathymetric segments, while gravimetric segment 6, 16, 17, 18, 20, and 21 are shorter (Figure 7).

Segments 16, 20, and 21 are bounded at one or both ends by nontransform discontinuities characterized by wide MBA highs with small saddle-shaped lows in the center (Figure 4). This configuration results in these segments being longer than corresponding gravimetric segments. Similarly, the MBA high at the eastern end of segment 18 is located a few kilometers to the west of the Novara ridge-transform intersection, while the MBA high at the western end of segment 14 is located a few kilometers to the east of the Melville ridge-transform intersection (Figure 4). We propose that this pattern is due, as proposed by *Prince and Forsyth* [1988] for local gravity lows observed in fracture zones of the Atlantic, to intense deformation and hydrothermal alteration reducing the density of crustal and upper mantle rocks in the transform region.

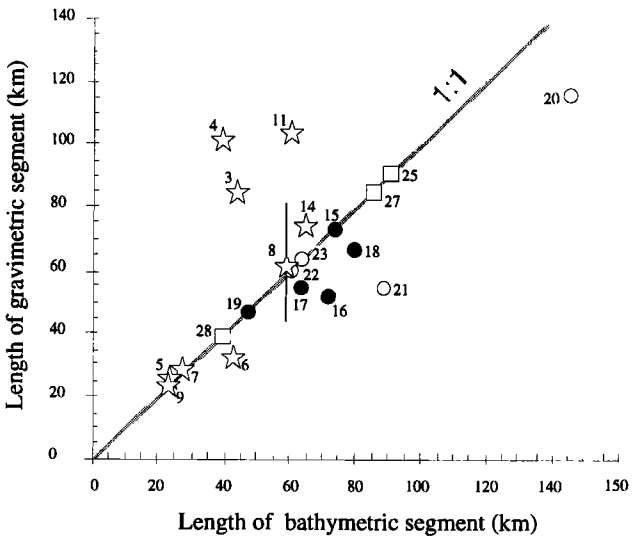

Figure 7. Length of gravimetric segments (as defined in Figure 6) versus the length of the corresponding bathymetric segments. Solid black line links the minimum and maximum values for the length of gravimetric segment 8 (see text). Stars, segments located to the east of the Melville transform; circles, segments located between the Gallieni and Melville transforms (solid circles, east of Atlantis II; open circles, west of Atlantis II); squares, segments located to the west of the Gallieni transform.

The length of gravimetric segment 8 is poorly constrained by available data because its western end coincides with a gap in the axial coverage (Figures 2 and 4). Axial MBA values may continue to increase westward to the higher values measured at the eastern end of segment 9 (Figure 4). This would make gravimetric segment 8 about 81 km long, with a ΔMBA of -24 mGal. Alternatively, axial MBA may reach a local maximum near the western termination of the bathymetric segment. This would make gravimetric segment 8 about 44 km long, for the same value of ΔMBA (Table 1).

The along-axis MBA low does not coincide with the topographic high in segments 3, 7, 8, 15, 18, 20, and 23 (Figure 4). In segment 23 the topographic high is probably an inside corner tectonic structure related to the Gazelle transform (Figure 4), and for the purpose of this study we have preferred to measure the relief of this segment from the top of the less prominent volcanic ridge that does coincide with the local MBA minimum (Table 1). We have done the same in segment 20, where the topographic high lies in the continuation of the off-axis trace of a discontinuity (Figure 2) and is inferred to be at least partly of tectonic origin. In segments 3, 7, 8, 15, and 18, however, seafloor morphology indicates that the central topographic highs are volcanic constructions [*Mendel et al.*, 1997; *Mendel and Sauter*, 1997].

3.3. Segment Length, Segment Relief, and MBA Variations

In this section, we discuss the formation of the axial topography, using the length and along-axis relief of bathymetric segments, and the length and ΔMBA of gravimetric segments as defined in Figure 6 and listed in Table 1. Errors made in measuring these values on bathymetry and MBA grids are small with regards to variations induced by the choices made in the definition of the axis, and in the location of segment centers and ends. We therefore chose not to produce error bars for these measurements. However, we take into account the smaller reliefs calculated for segments with prominent axial ridges by averaging axial depths and maximum axial depths (relief values between parentheses in Table 1). We allow for the length of gravimetric segment 8 to vary between 44 and 81 km as it is not better constrained by available gravity data. We also allow for the length of gravimetric segments 16, 17, 18, and 21 to vary between their actual length, and the (greater) length of corresponding bathymetric segments. The idea being that the gravity signal due to partial compensation of the topography in these segments is overprinted by the effect of intense deformation and hydrothermal alteration in transform and nontransform domains near the segments ends. By using the length of the corresponding bathymetric segment, we approach the length the gravimetric segment would have had without this

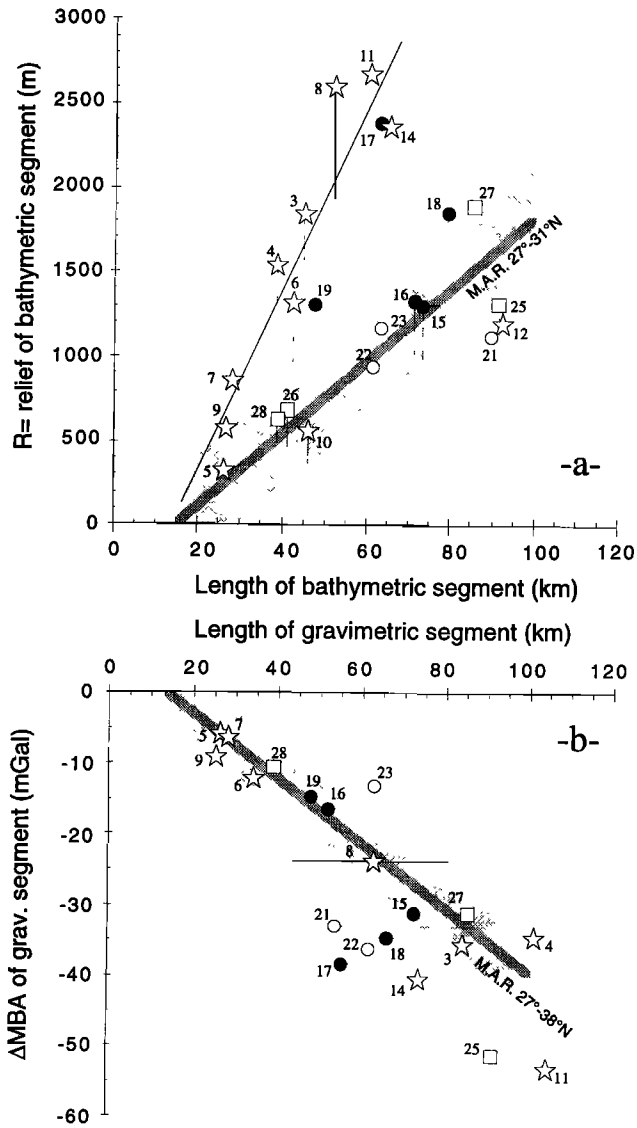

Figure 8. (a) Relief (R) versus length (L) of bathymetric segments. (b) Along-axis variations of mantle Bouguer gravity anomalies (ΔMBA) versus length of gravimetric segment. Symbols as in Figure 7. Thick grey lines are best fitting lines proposed for Mid-Atlantic Ridge segments by *Lin et al.* [1990] for Figure 8a (R = 0.0215L - 323; pale grey areas, +/- 300 m), and by *Detrick et al.* [1995] for Figure 8b (ΔMBA = 0.45L + 5; pale grey areas, +/- 5 mGal). The best fitting line (thin black line) for segments 3, 4, 5, 6, 7, 8, 9, 11, and 14 in Figure 8a is R = 0.054L - 765 (correlation coefficient: 0.916). Thin dotted lines in Figure 8a show range of values between the relief measured as shown in Figure 6, and the relief measured on an axial bathymetry profile that averages the axial depth and the maximum depth of the axial domain (as defined in Figure 3). Thin dotted lines in Figure 8b show minimum and maximum values of the length of gravimetric segment 8 (see text), and range of values between the length of gravimetric segments 16, 17, 18, and 21 (as defined in Figure 6). and the length of corresponding bathymetric segments (see text).

deformation and alteration effect. Finally, we do not include segment 20 in this analysis, because its present-day length appears to result from the recent, and possibly ephemeral, propagation of a volcanic ridge into a nontransform discontinuity.

Compared to segments of the MAR [*Lin et al.*, 1990; *Neumann and Forsyth*, 1993; *Detrick et al.*, 1995; *Thibaud et al.*, 1998], segments of the studied portion of the SWIR have similar lengths (20 to 100 km except for segment 20), a similar range of along-axis MBA variations (ΔMBA down to -53 mGal), but a wider range of along-axis reliefs (up to 2672 m; Table 1). Segments 3, 4, 11, and 14 have high reliefs and large ΔMBA (Figure 8), and their gravity signature has a longer length than the topography (Figure 7). Segment 8 is another high-relief segment of the east of Melville region, but it has a smaller ΔMBA, and the length of its gravity signal is not well constrained. Segment 17 is the only segment west of Melville with a relief greater than 2000 m (Figure 8a).

The relief (R) and the length (L) of MAR segments are roughly correlated [*Blackman and Forsyth*, 1991; *Lin et al.*, 1990; *Neumann and Forsyth*, 1993; *Thibaud et al.*, 1998], mean along-axis slopes ($R/(L/2)$) varying between 20 and 40 m/km. It is clear that most SWIR segments from the region east of Melville have higher relief to length ratios [*Mendel et al.*, 1997] (Figure 8a), corresponding to mean along-axis slopes of up to 90 m/km. The exceptions are segments 10 and 12, which do not have a gravity signature, and segments 5 and 9 which are only 26 km long. By contrast, most segments west of Melville have mean along-axis slopes comparable to those of MAR segments (Figure 8a). The exception there is segment 17, and to a lesser extent segments 18, 19, and 27, which have steeper mean along-axis slopes. Segments 21 and 25 have mean along-axis slopes of less than 30 m/km.

Segments of the MAR also show a correlation [*Kuo and Forsyth*, 1988; *Lin et al.*, 1990; *Blackman and Forsyth*, 1991; *Lin and Phipps Morgan*, 1992; *Neumann and Forsyth*, 1993; *Detrick et al.*, 1995; *Wang and Cochran*, 1995; *Thibaud et al.*, 1998] between segment length and ΔMBA (Figure 8b). This correlation corresponds to along-axis mean MBA gradients (ΔMBA/(L/2)) of 0.6 to 0.8 mGal/km. Most gravimetric segments from the SWIR have similar mean MBA gradients (Figure 8b). Segments 11, 14, 17, 18, 21, 22, and 25, however, have stronger along-axis mean MBA gradients (up to 1.4 mGal/km), and segment 23 has a mean MBA gradient of only 0.5 mGal/km.

Stronger mean along-axis MBA gradients indicate that the density structure varies along-axis more rapidly than in other segments. This suggests a more rapid along-axis increase of crustal thickness and/or of mantle temperature and melt content. Many segments with strong mean MBA gradients also have steep mean along-axis slopes (segments 11, 14, 17, and 18; Figure 8). Conversely, segments 3 and 4 have mean along-axis slopes greater than 78 m/km, but mean MBA gradients of only 0.6 to 0.8 mGal/km, and segments 21, 22, and 23 have strong mean MBA gradients but moderate to small mean along-axis slopes (Figure 8a). The length of the MBA signature of segment 8 (one of the highest relief segment in the study area; Figure 8a), and therefore its along-axis MBA gradient, are unfortunately not well constrained.

3.4. Along-Axis Crustal Thickness Variations

Mantle Bouguer anomalies include components due to variations in crustal thickness, to variations in crustal density, and to variations in mantle density. We do not have enough off-axis gravity and bathymetry data to produce a grid of residual MBA from which we could then derive crustal thickness variations in the study area. We therefore resorted to a crude analytical method and calculated variations in crustal

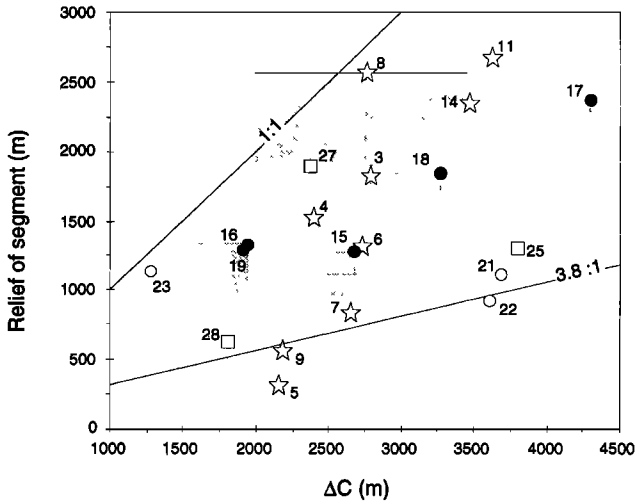

Figure 9. Segment relief (R) versus the amplitude of crustal thickness variations (ΔC), calculated for each segment assuming that along-axis variations of mantle Bouguer gravity anomalies (ΔMBA) result from sinusoidal topography at the crust-mantle interface (see Appendix A). Symbols as in Figures 7 and 8. Thin dotted lines and pale grey areas correspond to the same range of variation in axial relief and in the length of gravimetric segments as in the diagrams of Figure 8.

thickness (ΔC) within each segment, assuming that the gravity signal is caused by sinusoidal variations in the thickness of a constant density crust (ρ_c = 2700 kg/m^3) overlying a constant density mantle (ρ_m = 3300 kg/m^3). In this calculation, ΔC is related to ΔMBA through a factor (see Appendix A) that depends on the wavelength of MBA variations (i.e., the length of each gravimetric segment). The position of the various segments in Figure 9 is therefore a direct reflection of their position in the two diagrams of Figure 8.

The validity of this approach is dependent on how closely MBA variations approach a sinusoidal curve. It is apparent in Figure 4 that, in many segments, MBA variations are V-shaped instead of being sinusoidal: this will bias ΔC estimates toward higher values. Another, and potentially a more important, problem is the continuation of the periodic pattern in the third dimension (perpendicular to the axis). Off-axis MBA data are scarce, but the lack of a regular off axis peak and trough pattern in the satellite FAA map to the east of Melville and to the west of Gallieni (Figure 1) suggests that crustal thickness at a given location along the ridge in these regions can vary over a relatively short timescale (this will bias ΔC estimates toward lower values). Finally, this approach does not take into account along-axis variations in mantle density due to the colder thermal regime near axial discontinuities and to possibly higher melt contents near segments centers: this will bias ΔC estimates toward higher values.

ΔC values shown in Figure 9 must be appreciated in the light of these limitations. More reliable ΔC values will only be obtained through three-dimensional (3-D) models (requiring additionnal off-axis gravity and bathymetry data), instead of the 2-D model used here. ΔC varies between 3.5 km and more in segments 11, 14, 17, 21, 22, and 25, and 2 km and less in segments 16, 19, 23, and 28. ΔC values calculated for segments 7 and 8 are within these two bounds and can be checked against actual seismic crustal thicknesses [*Muller et al.*, 1998]. The seismic crustal thickness decreases by about 2.5 km, and the average seismic velocity of the crust diminishes between the center and the ends of these segments [*Muller et al.*, 1998]. Values of ΔC calculated from gravity data for segments 7 and 8 are of the same order. The decrease in crustal velocities observed toward segment ends has been documented previously along the MAR [*Tolstoy et al.*, 1993; *Detrick et al.*, 1995]. It probably goes together with a decrease of crustal densities and should therefore cause ΔC calculated from gravity data to be underestimated [*Tolstoy et al.*, 1993; *Detrick et al.*, 1995]. However, our crude method of calculating ΔC does not take into account the effect of having a colder, denser mantle at the ends of the segment, and this could balance the effect of these along-axis variations in crustal density.

3.5. Along-Axis Variations of the Depth of the Axial Valley and the Mode of Compensation of the Axial Relief

The axial relief (R) of a slow spreading ridge segment can be seen as the addition of two components: the isostatic response of the axial lithosphere to loads emplaced above, within, or below the plate (Ri); and rifting of the axial lithosphere producing a dynamically supported axial valley that deepens toward the segment's ends (Rv). If we could remove this dynamically supported component of the axial relief and consider only the response to isostatic loads (Ri) versus ΔC, the 1:1 line in the resulting diagram (Figure 10) would correspond to an uncompensated relief sitting on a plate without deflecting it, the 3.8:1 line would correspond to Airy isostatic compensation ($\Delta C = ((\rho_m - \rho_w)/(\rho_m - \rho_c))R$), and the Ri:0 baseline would correspond to an uncompensated negative load located under the plate.

Domains between the 1:1 and 3.8:1 lines, and below the 3.8:1 line in Figure 10, could then correspond to partial isostatic compensation of positive loads emplaced above the

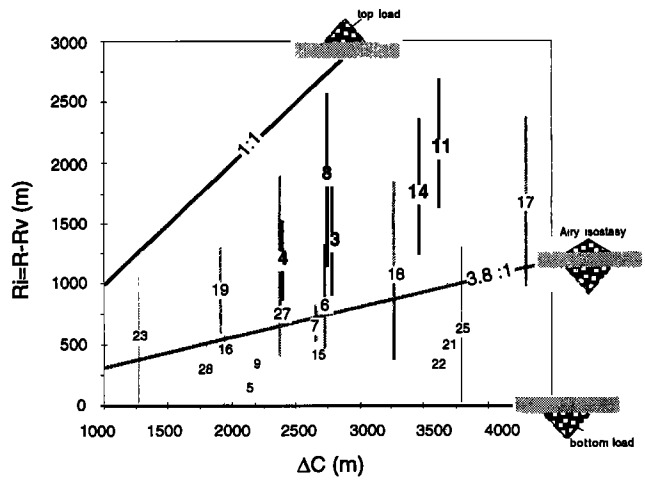

Figure 10. Range of values discussed in text for the isostatic response component (Ri) of the axial relief (R), versus the amplitude of crustal thickness variations (ΔC), calculated for each segment assuming that along-axis variations of mantle Bouguer gravity anomalies (ΔMBA) result from sinusoidal topography at the crust-mantle interface (see Appendix A). Ri is inferred to be what is left of total relief (R) after removal of the component due to the dynamically supported axial valley (Rv). The Ri:0 baseline corresponds to crustal thickening loading a rigid plate from underneath. The 1:1 line corresponds to relief sitting on a rigid plate. The 3.8:1 line corresponds to Airy isostatic compensation.

plate (plate rigidity prevents the topography in the center of the segment to be as deep as it would be in a local isostatic compensation mode) and of negative loads emplaced below the plate (plate rigidity prevents the topography in the center of the segment to be as high as it would be in a local isostatic compensation mode), respectively. We unfortunately do not have sufficient constraints on the values of *Rv* in our study area to actually plot each segment on this *Ri* versus ΔC diagram. This would require sufficient knowledge of lithospheric rheology and thermal structure to model axial valley depths and their along-axis variations [*Neumann and Forsyth*, 1993; *Shaw and Lin*, 1996]. Specifically, we have no constraints on the thermal and mechanical effect of the broad and large offset nontransform discontinuities that are typical of the very slow spreading SWIR, nor do we have natural seismicity constraints on axial lithospheric thickness along this ridge.

The range of *Ri* values shown in Figure 10 extends from *Rv* equal zero (*Ri* = *R*), an improbable end-member given the occurrence of well-developed nodal basins at the end of most SWIR segments [*Mendel et al.*, 1997] (Figure 5), to *Rv* equal *R* minus the mean along-axis relief of a MAR segment of similar length (thick grey line in Figure 8a). This range of *Ri* values is based on two assumptions: (1) that *Rv* values for segments of the SWIR should be similar to *Rv* values of MAR segments of similar lengths; and (2) that the *Rv* value of a MAR segment is at the most equal to the whole measured relief (*R*) of this segment. This second assumption is consistent with the conclusions of thermomechanical modeling of MAR axial valley depths by *Neumann and Forsyth* [1993]. The first assumption is based on the observation that along-axis MBA gradients in most SWIR segments are similar to those of MAR segments (thick grey line in Figure 8b). This suggests that, for a given segment length, the contrast in lithospheric and crustal thickness between the center and the extremities of a segment is similar at the SWIR and at the MAR. Because variations of the depth of the axial valley are thought to be caused by along-axis variations of axial lithospheric thickness and crustal rheology [*Phipps Morgan et al.*, 1987; *Lin and Parmentier*, 1989; *Chen and Morgan*, 1990; *Neumann and Forsyth*, 1993; *Shaw and Lin*, 1996], similar MBA gradients suggest that the axial valley component (*Rv*) of the axial relief is of the same order of magnitude at the SWIR and at the MAR.

The range of *Ri* values shown in Figure 10 for high relief segments east of Melville (segments 3, 4, 8, 11, and 14) and for segments 17 and 19 between Melville and Atlantis falls entirely or almost entirely between the 1:1 and 3.8:1 lines, suggesting a predominant role of top loads in the isostatic response of the axial region. By contrast, the range of *Ri* values for lower relief segments (segments 5 and 9 east of Melville and segments 21, 22, 25, and 28 west of Atlantis) falls almost entirely beneath the 3.8:1 line, suggesting a predominant role of bottom loads. Flexural response to loads emplaced above the plate could also explain the difference in length of gravimetric and bathymetric segments 3, 4, 11, and 14 (Figures 7 and 11). In terms of geology, a dominance of top loads suggests a higher relative contribution of volcanic constructions loading the plate from above, with respect to crustal material or lighter mantle emplaced at deeper levels within or beneath the plate, to along-axis crustal thickness variations. In high relief segments east of Melville, and in segments 17 and 19 between Melville and Atlantis, the contribution of the uppermost, effusive, part of the crust to along-axis MBA variations would therefore be greater than in the other segments of the studied area (Figure 11).

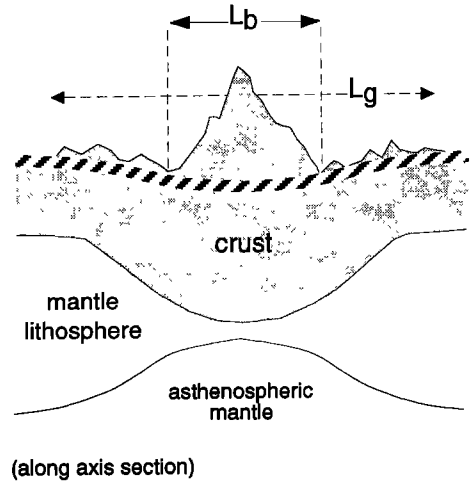

Figure 11. Schematic along-axis section of a high relief SWIR segment east of the Melville transform. A large axial volcanic construction loads the plate and deflects it. Thick hatched line, top of deflected plate. Additional loading at Moho level (thickening of crust at segment center) and in upper mantle (thinner mantle lithosphere and possibly lighter asthenospheric mantle beneath segment center) also contribute to along-axis variations of mantle Bouguer gravity anomalies. Length of the bathymetric segment (*Lb*) is shorter than length of the corresponding gravimetric segment (*Lg*) due to flexural response of the plate and to along-axis extent of Moho and sub-Moho loads. Thinning of mantle lithosphere at segment center is due to excess magmatism causing the axial thermal regime to be hotter there. Asthenospheric mantle may be lighter beneath segment center due to higher temperatures and larger melt content.

The existence of volcanic constructions that load the axial lithosphere from above in segments 3, 4, 8, 11, 14, 17, and 19 is also consistent with observations made on bathymetric maps (Figures 5b and 5c). The axial valley floor in these segments does not have an hourglass shape [e.g., *Sempéré et al.*, 1993]. Instead, it has a width (measured in a north-south direction, parallel to spreading) of 10 to 20 km over most of the segment length [*Mendel et al.*, 1997], and it does not narrow (as in the hourglass shape) near the center of the segment but appears to be filled by rounded or elongated reliefs that bear numerous volcanic cones [*Mendel and Sauter*, 1997]. This setting suggests that topographic highs in the center of these segments do not represent the floor of a narrow and shallow axial valley but are volcanic edifices filling a rather wide and deep axial valley.

4. Regional Variations in Axial Depth, Melt Thickness and Mantle Temperature

Long-wavelength variations in axial depths reflect regional changes in the axial density structure, which is controlled by crustal thickness and by the density of the underlying mantle. The large-scale eastward deepening of the axis in the study area (Figure 4) therefore suggests that average crustal thicknesses and/or mantle temperatures beneath the ridge decrease from west to east. In this section we relate magma

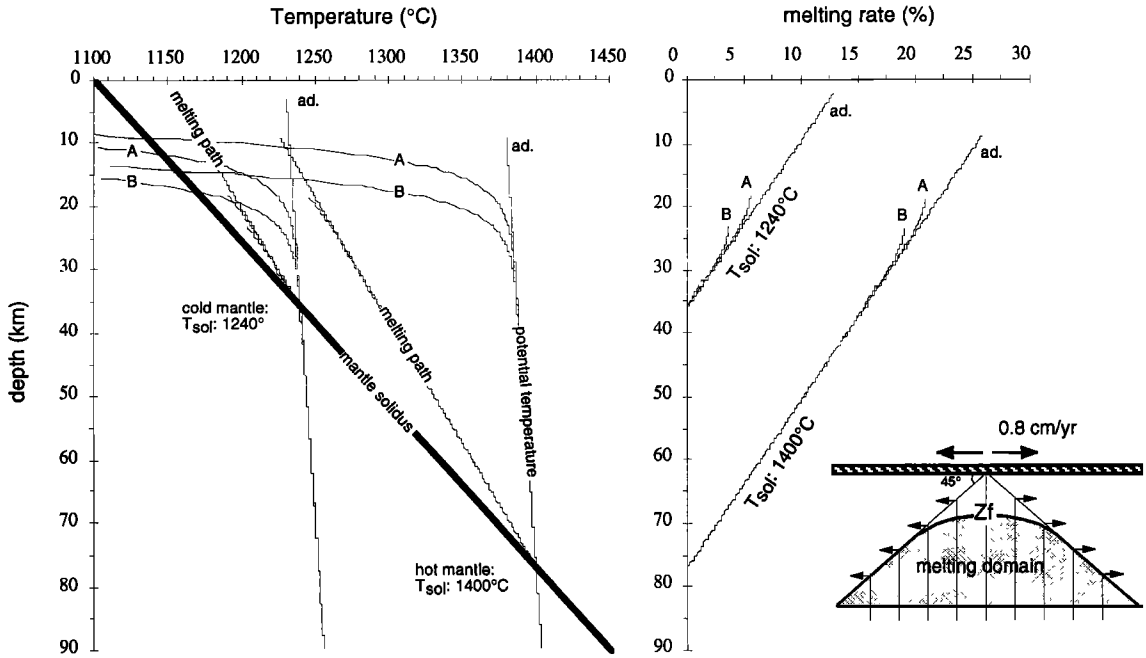

Figure 12. Temperatures and melting rates calculated as a function of depth with the 1-D conductive cooling and melting model outlined in Appendix B, for two end-member mantle temperatures at solidus: cold mantle (T_{sol} = 1240°C) and hot mantle (T_{sol} = 1400°C). Cases A and B correspond to two conductive cooling settings (see text and Appendix B). Temperatures and melting curves for adiabatic (ad.) melting are shown for comparison. The sketch shows the geometry of the conductive cooling and melting model, with a wedge angle of 45° and a mantle upwelling velocity equal to the half spreading rate. Z_f is the depth at the top of the melting domain.

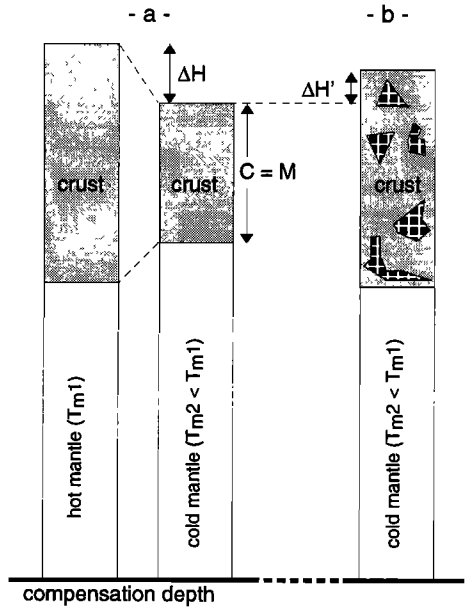

Figure 13. Sketch of isostatically balanced columns for the calculation of regional axial depths. (a) The crust is made only of magmatic rocks. ΔH (difference in regional axial depth) therefore results only from differences in melt thickness (M = crustal thickness) and in mantle temperature (see Appendix B). (b) The crust also includes a proportion (S) of serpentinized mantle-derived peridotites (black squares). $\Delta H'$ relative to a setting with similar mantle temperature and melt thickness but no serpentinites in the crust is expressed as $(\rho_m - \rho_c) / (\rho_m - \rho_w)$ $M S / (1 - S)$.

budget, mantle temperature, and regional axial depth, in order to better constrain what regional changes in mantle temperature and magma supply may accompany the changes observed in the axial segmentation pattern across the Melville fracture zone. We make the following hypotheses: - that the rate of decompression melting in the mantle at any given depth above the solidus is proportional to the difference between the solidus temperature, and the temperature that would prevail at that depth had no melting occurred (Figure 12); - that the regional pattern of mantle upwelling beneath the SWIR corresponds to passive flow (this assumption does not preclude active mantle flow at the scale of segments); - that regional variations in axial depths are isostatically compensated within the crust and the upper 200 km of the mantle (Figure 13).

Previous models relating regional axial depths to magma budget and mantle temperature [*Klein and Langmuir*, 1987; *Ito and Lin*, 1995] are based on the same hypotheses and also assume that the crust is a purely magmatic layer. This does not fit with the frequent sampling of serpentinized peridotites in the axial valley of the SWIR to the east of the Gallieni transform [*Mével et al.*, 1997]. In Figure 13b, we offer an alternative way to relate regional axial depths to crustal thickness and mantle temperature, as a function of the proportion (S) of serpentinized peridotites in the crust.

4.1. Mantle Melting Model

Our mantle melting model differs from those of *Klein and Langmuir* [1987] and *Ito and Lin* [1995] in that it did not seem realistic to assume adiabatic melting all the way up to the

base of the crust of this very slow and presumably cold ridge [*Reid and Jackson*, 1981; *Bown and White*, 1994; *Sleep and Barth*, 1997]. We therefore made our calculations for a range of potential mantle temperatures corresponding to three axial thermal regimes: a perfectly adiabatic mantle upwelling regime that represents a hot and unlikely end-member and two conductive cooling settings in which potential temperatures are calculated using a crude, 1-D analytical method (see Appendix B), with a mantle upwelling velocity equal to the half spreading rate (0.8 cm/yr) and two sets of boundary conditions meant to introduce the effect of variable degrees of hydrothermal cooling: a temperature of 500°C is fixed at a depth of 5 km in setting A and at a depth of 10 km in setting B. For comparison, earthquake epicenter depths at the faster spreading MAR suggest that temperatures corresponding to the base of the brittle lithosphere (estimated to correspond to temperatures of 400° to about 800°C depending on the lithology [*Kirby*, 1983]) are reached at depths of 3 to 9 km [*Toomey et al.*, 1988; *Kong et al.*, 1992; *Wolfe et al*, 1995]. *Huang and Solomon* [1988] present teleseismic data suggesting similar epicenter depths for the SWIR.

In a passive flow regime, mantle upwelling velocities vary with the wedge angle of the axial melting region, a probable function of spreading rate and mantle viscosity [*Spiegelman and McKenzie*, 1987]. We chose an upwelling velocity of 0.8 cm/yr at the SWIR (i.e., equal to the half spreading rate), corresponding to a fixed wedge angle of 45° (Figure 12), and therefore neglect the effect of variable mantle viscosity. Our crude 1-D analytical melting model (see Appendix B) nonetheless yields similar temperature profiles in the melting domain to the more elaborate 2-D numerical model of *Bown and White* [1994]. It also allows for analytical calculations of the extent of melting and of the magma budget (melt thickness) following the simple method described in Figure 50 of *Langmuir et al.* [1992]. Melting parameters (latent heat of melting, solidus slope, and dT/dF; see Appendix B) used in our model are such that a melt thickness of 6 km is produced by adiabatic melting with a mantle temperature at solidus of 1342°C. Other models have used different parameters and obtained different values for this "normal" mantle temperature (e.g., 1300°C [*Bown and White*, 1994]). Because there is considerable uncertainty on which melting parameters are most appropriate (see discussion of *Langmuir et al.* [1992]), these calculated mantle temperatures should not be taken at face value but used to assess relative changes in the temperature of the mantle beneath different ridge regions.

Calculated profiles of temperature and extent of melting as a function of depth are shown in Figure 12 for two end-member mantle solidus temperatures (cold mantle, 1240°; and hot mantle, 1400°C). Final depths of melting correspond to the base of the crust in the adiabatic setting and to depths of about 18 and 23 km in conductive cooling settings A and B,

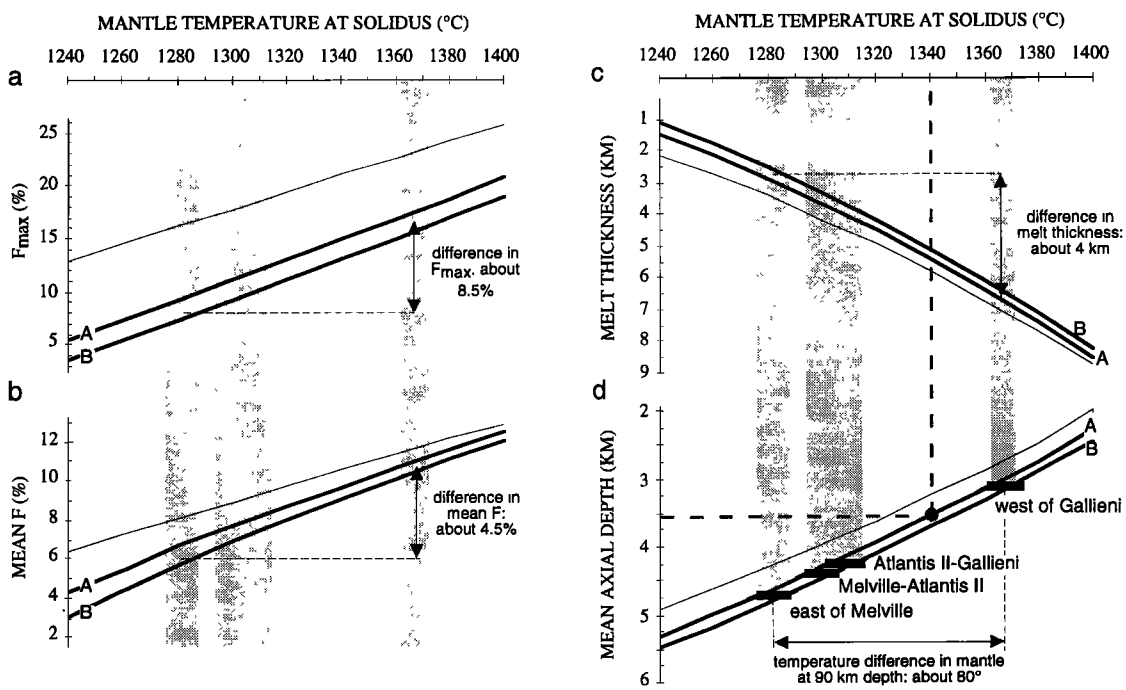

Figure 14. (a) Maximum extent of mantle melting (F_{max}), (b) mean extent of mantle melting (Mean F), (c) melt thickness, and (d) mean axial depth, calculated as a function of the temperature of the mantle at solidus (see text and Appendix B). Thin lines, adiabatic melting. Thick lines, conductive cooling settings A and B (see text and Appendix B). Black rectangles in Figure 14d show the range of calculated mantle solidus temperatures (for conductive cooling settings A and B) that fit observed regional depths in the four regions of the study area. Pale grey domains in Figures 14a-14d correspond to this range of mantle temperatures. Fit is achieved with a compensation depth of 200 km and a reference column with an axial depth of 3550 m, 5.5 km of crust, conductive cooling setting A, and a temperature of the mantle at solidus of 1340°C (grey dot in Figure 14d). The full range of variation in mantle solidus temperatures between the deepest ridge region east of Melville, and the shallowest ridge region west of Gallieni, corresponds to a difference of about 80° in the calculated temperature of the mantle at a depth of 90 km (Table 2).

respectively. These final depths of melting vary very little with initial mantle solidus temperature. The mean depth of melting and the maximum extent of melting (F_{max}; Figure 14a) both vary significantly, at a given mantle solidus temperature, with the axial cooling regime. By contrast, the mean extent of melting (mean F) is mostly controlled by the mantle solidus temperature (Figure 14b). For example, at mantle solidus temperatures greater than about 1320°C, mean F varies by less than 2% between the adiabatic regime and our coldest conductive cooling regime (Figure 14b).

The melt thickness (equivalent to crustal thickness if all the melt is extracted from the mantle and if the crust is purely magmatic) is calculated using mean F, and the height of the mantle column above the solidus [see *Langmuir et al.*, 1992]. Similarly to mean F, it is more sensitive, for a mantle upwelling velocity of 0.8 cm/yr, to mantle solidus temperatures than to the mantle cooling regime (Figure 14c). The difference in melt thickness computed for a mantle solidus temperature of 1340°C, between the adiabatic cooling regime (independent of spreading rate) and conductive cooling setting B is only 12% (5.85 against 5.13 km). It increases to 50% (2.13 against 1.07 km) for a very cold mantle solidus temperature of 1240°C (Figure 14c). As previously noted by *Bown and White* [1994], the model therefore does not predict a drastic decrease of melt thickness due to enhanced conductive cooling of the mantle at the slow spreading SWIR, except if the mantle temperature at solidus is exceptionaly cold.

4.2. Regional Axial Depth, Mantle Temperature, and Melt Production

Relative variations in axial depth are calculated for each mantle solidus temperature, assuming that isostatic balance is achieved with a compensation depth arbitrarily set as 200 km (Figure 13 and Appendix B). We then calculate absolute variations in axial depths as a function of mantle solidus temperatures (Figure 14c), assuming first that the crustal thickness equals the melt thickness (i.e., no serpentinized peridotites in the crust; Figure 13a), and using a reference column with an axial depth of 3550 m, 5.5 km of crust, a temperature of the mantle at solidus of 1340°C, and conductive cooling setting A. In this setting, regional axial depths east of the Melville fracture zone (4730 m), between Atlantis II and Melville (4430 m), between Gallieni and Atlantis II (4230 m), and west of the Gallieni fracture zone (3090 m), correspond to calculated mantle temperatures at the solidus of 1275° to 1363°C for conductive setting A, and of 1285° to 1371°C for conductive setting B (Table 2 and Figure 14d). Mean extents of melting calculated for settings A and B (Table 2 and Figure 14b) are 6 to 6.4% for the region east of Melville, and 7 to 7.4%, 7.7 to 7.9%, and 10.6 to 10.8%, respectively, for the Atlantis II to Melville, Gallieni to Atlantis II, and west of Gallieni regions. The resulting melt thickness (Table 2 and Figure 14c) is about 2.7 km for the region east of Melville, and 3.4, 3.9, and 6.6 km, respectively, for the Atlantis II to Melville, Gallieni to Atlantis II, and west of Gallieni regions.

Mid-ocean ridge basalt compositions can also be used, provided that assumptions are made about the composition of the mantle source, on partition coefficients, and about the modes of melt extraction, to estimate mean extents of melting in the mantle beneath the ridge [*Klein and Langmuir*, 1987; *White et al.*, 1992]. Mean F of about 6%, 8%, and 11% can be estimated using the method of *Klein and Langmuir* [1987] (see Appendix B), from the sodium content of a small collection of basalts sampled east of Melville (segments 7 and 8; $Na_{8.0}$ about 3.7% [*Robinson et al.*, 1996]), east of Atlantis II (segment 19; $Na_{8.0}$ about 3.2% [*Robinson et al.*, 1996]), and west of Gallieni (segment 27; $Na_{8.0}$ about 2.5% [*C. Mével et al.*, unpublished results, 1997]), respectively. These values are comparable to those listed in Table 2 for these regions.

The average seismic crustal thickness for three along-axis and across-axis seismic profiles made over segments 7 and 8 (65°E to 66°45'E) is 3.8 to 4.3 km [*Muller et al.*, 1998], a bit more than the 2.7 km calculated in our model. This calculated value agrees better with the melt thickness estimated for the same area based on the major and trace element composition of dredged basalts (1.5 to 2.5 km [*Robinson et al.*, 1996]). The 3.4 km melt thickness estimated in this section for the Atlantis II to Melville region is also a bit less than seismic crustal thicknesses determined in the walls of the Atlantis II transform away from the Atlantis Platform (4 km [*Muller et al.*, 1997]). Such discrepancies have been attributed to the incorporation of a component of partially serpentinized peridotites into the crust [*Muller et al.*, 1997; *Sleep and Barth*, 1997; *Minshull et al.*, 1998]. There are large uncertainties attached to both seismic modeling, and melt thickness calculations, be they based on regional depths or on basalt composition, so that it would not be wise to use these discrepancies to directly quantify the proportion of serpentinized peridotites that may be present in the crust. For example, changing the compensation depth from 200 to 300 km in the cold region east of Melville leads to a 400 m increase in the melt thickness computed for conductive setting A (3.1 instead of 2.7 km) for a mantle temperature at solidus of 1286°C (instead of 1275°C; Table 2).

Melt thicknesses calculated in this section are regional averages that integrate segment scale variations in magma

Table 2. Regional Axial Depth, Temperature of the Mantle at Solidus (Tsol) and at a Depth of 90 km (T(90 km)), Maximum Extent of Melting (F max), Mean Extent of Melting (mean F), and Melt Thickness Calculated in Figure 14 for the Four Studied Regions of the SWIR

	East of Melville, 4730 m*		Melville to Atlantis II, 4430 m		Atlantis II to Gallieni, 4230 m		West of Gallieni, 3090 m	
	A+	B+	A	B	A	B	A	B
Tsol, °C	1275	1285	1293	1302	1304	1313	1363	1371
T(90km), °C	1288	1297	1305	1313	1315	1324	1370	1377
F max, %	8 9	8	10 6	9.5	11.6	10 6	17 3	16 2
Mean F, %	6 4	6	7 35	7	7 9	7 7	10 8	10.65
Melt thickness, km	2 7	2 7	3 4	3.4	3 85	3 9	6 6	6 7

* Regional axial depth

+ Conductive cooling settings A and B.

supply. Segment scale crustal thickness variations calculated from MBA variations for the region east of Melville and for the region west of Gallieni are similar (Figure 9) , while calculated regional melt thicknesses are of the order of 2.7 and 6.6 km, respectively (Table 2).This suggests if segment scale crustal thickness variations are indeed the principal cause of along-axis MBA variations [e.g., *Kuo and Forsyth*, 1988; *Lin et al.*, 1990] that a larger proportion of the magma that is extracted from the mantle is focused toward the center of segments in cold than in hotter regions of the SWIR.

4.3. Effect of Having Serpentinized Peridotites in the Crust

The effect of having serpentinized peridotites in the crust is summarized in Figure 13b: it thickens the crust so that for a given mantle temperature and melt thickness, regional axial depths will be shallower. In our case, the regional axial depth is the observable, while mantle temperature, melt thickness, and the average proportion of serpentinized peridotites in the crust are the unknown variables. For a given regional axial depth, the computed mantle temperature, mean F, and melt thickness will decrease as the average proportion of serpentinized peridotites in the crust increases. In Figure 15 we allow this proportion to range between 0 and 50% of the total crustal thickness and show the evolution of mantle temperatures at solidus, mean F, and melt thickness calculated for the four studied ridge regions, with conductive setting A. Serpentinized peridotites have not been dredged west of the Gallieni fracture zone. This does not necessarily mean that they are absent in the crust of this region, as dredging there was sparse [*Mével et al*, 1997], but it is likely that they are less abundant than in the colder and deeper regions further to the east. By contrast, serpentinized peridotites have been dredged repeatedly in the three regions east of Gallieni [*Mével et al*, 1997]. Allowing the average proportion of serpentinized peridotites in the crust to vary between 0 and 50% within each of these three regions leads to variations of up to 35° in the calculated mantle temperatures at solidus (Figure 15a), of up to 1.5 km in melt thickness (Figure 15b), and of up to 2% in mean F (Figure 15c). These variations are of the same order of magnitude as those associated with a 500 m change in regional axial depth (e.g., between the east of Melville and the Gallieni to Atlantis II regions; Table 2) with a crust made only of magmatic rocks. This means that the proportion of serpentinized peridotites in the crust is an important variable that should be taken into account when using regional axial depths to derive mantle temperatures and melt parameters at slow spreading ridges.

4.4. Effect of Ridge Obliquity

The ridge obliquity (ϕ) is another potential source of regional variations in crustal thickness and extent of melting in the study area. For a given spreading rate, and a constant geometry of passive mantle upwelling, the upwelling velocity should decrease as ϕ increases, by a factor equal to $\cos\phi$. Ridge obliquity (Figure 2) varies between 0° (segments 9 to 11) and about 40° (segments 3 to 8 and 15 to 17). Within our simple mantle upwelling and melting model, this corresponds to a decrease of the upwelling velocity from 0.8 cm/yr (ϕ = 0°) to 0.6 cm/yr (ϕ = 40°). The effect of this decrease is maximum if the mantle is cold but remains small. For a very cold mantle (1240°C at the solidus), mean F (calculated for conductive setting A) decreases from 4.3% (at 0.8 cm/yr), to 3.3% (at 0.6 cm/yr), and the melt thickness decreases from 1.48 to 1.13 km.

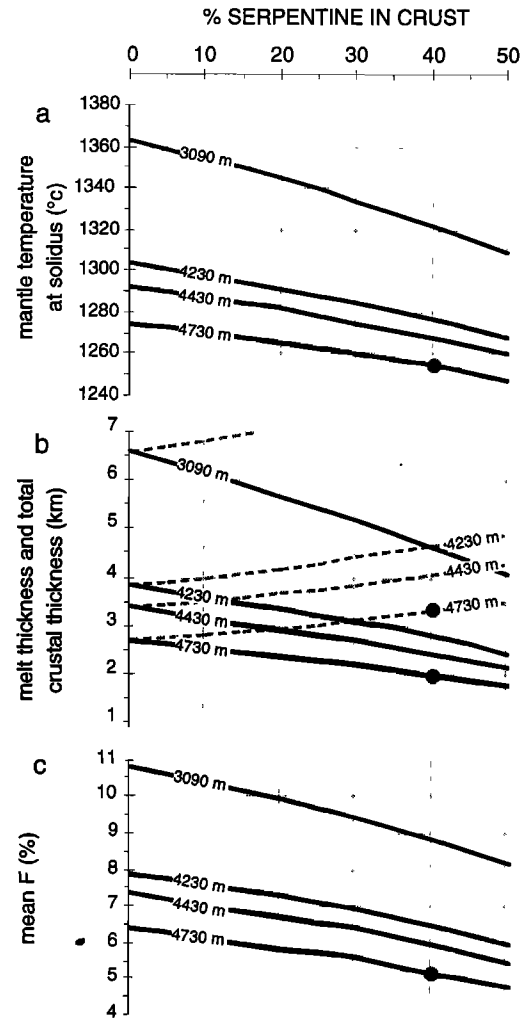

Figure 15. (a) Mantle temperature at solidus, (b) melt thickness (solid line) and total crustal thickness (dashed line), and (c) mean extent of mantle melting (mean F), calculated for conductive setting A (see Appendix B), as a function of the proportion (S) of serpentinized mantle-derived peridotites in the crust (see Figure 13b) for regional axial depths measured in the four regions of the study area (Table 2). These diagrams are constructed by adjusting the mantle temperature at solidus, and consequently the melt thickness, for each value of S so that axial depths remain constant. For example (dark grey circles in Figures 15a-15c), if the crust along the ridge east of Melville contained 40% serpentinized peridotites, it would have a total thickness of 3.4 km for a 2 km melt thickness (Figure 14b), the corresponding mantle temperature at solidus would be 1255°C (Figure 14a), and the mean extent of melting would be only 5.2% (Figure 14c).

For a mantle temperature of 1340°C at the solidus, the effect has become even smaller: mean F decreases from 9.7% (at 0.8 cm/yr), to 9.2% (at 0.6 cm/yr), and the melt thickness from 5.45 to 5.2 km.

5. Discussion

5.1. How Can Large Volcanic Constructions Be Formed at the Ridge Axis?

The building of large volcanic constructions at a ridge axis requires that the axial lithosphere be thick enough to support

these constructions, a condition that should not be a problem at a very slow spreading and magma deprived ridge such as the SWIR east of Melville. It also requires a significant proportion of the magma supplied to the ridge to be channeled through the axial lithosphere to build volcanoes on the seafloor, instead of forming sills or plutons at mid to lower crustal levels, as proposed in many geological models of slow-spread crust [e.g., *Dick*, 1989; *Sinton and Detrick*, 1992; *Cannat*, 1993; *Phipps Morgan and Chen*, 1993]. Magma transport from its freezing depth (the depth at which axial temperatures are such that magma starts crystallizing), up to near the seafloor must therefore be rapid, so that only a small part of the magma crystallizes en route, and driven by magma overpressures high enough to overcome nonlithostatic stresses in the lithosphere. The most rapid way to transport magma is through dikes, and large magmatic overpressures can be produced by lithostatic stresses provided that the dike is open over a sufficient height in host rocks that are denser than the magma [*Lister and Kerr*, 1991].

In the setting proposed in Figure 16, magma pools at the freezing horizon, corresponding roughly to the base of the ductile lithosphere. This influx of magma that starts crystallizing releases heat so that the base of the lithosphere, and the freezing horizon, become shallower wherever most melt has gathered. Magma migrates along this sloping horizon [*Sparks and Parmentier*, 1991], both across and along-axis, and gathers beneath what then becomes the center of a ridge segment. Dikes initiate in the melt-rich region near the freezing horizon, as described by *Sleep* [1988]. Some of these dikes stop their upward propagation and feed sills within the upper mantle and lower crust, producing gabbros and dolerites, while others propagate all the way up, either as single dikes, or more likely as series of relays. These shallow dikes propagate laterally in the direction perpendicular to spreading [*Rubin and Pollard*, 1987; *Lister and Kerr*, 1991], feed fissural eruptions, and form the east-west volcanic ridges and numerous volcanic cones that characterize the center of high relief segments in the east of Melville area [*Mendel and Sauter*, 1997].

Compared with the MAR, or with the SWIR west of Melville, the SWIR east of Melville has an unusual segmentation pattern with a few very high relief segments, a very low magma supply, and a cold subaxial mantle. It seems like a workable hypothesis that these three characteristics are somehow related. We thus need a mechanism by which magma would be more likely to be rapidly transported upward in dikes in a thick, cold, and magma deprived axial lithosphere, while melts would be more likely to stall at depth and form gabbroic and doleritic intrusions in a more magmatic axial environment. At least two adequate mechanisms can be found in the literature: (1) that repeated injections of magma modify the stress field in the lower crust so that subsequent dikes turn into sills there [*Gudmundson*, 1990] and (2) that repeated injections of magma heat the lower crust so that a weak ductile zone develops there, in which the vertical gradient of horizontal stress (lithostatic stress minus the rock strength for an environment that undergoes steady extension) is less than that above or below, favoring lateral, instead of vertical, dike propagation [*Rubin*, 1990]. In these two mechanisms, the critical factor is the frequency of magma injections, a parameter that, for a given spreading rate, could vary with the ridge's melt supply. If the melt supply is high, dike injections could be more frequent and the formation of sills could be favored. If the melt supply is low, dike injections could be less frequent,

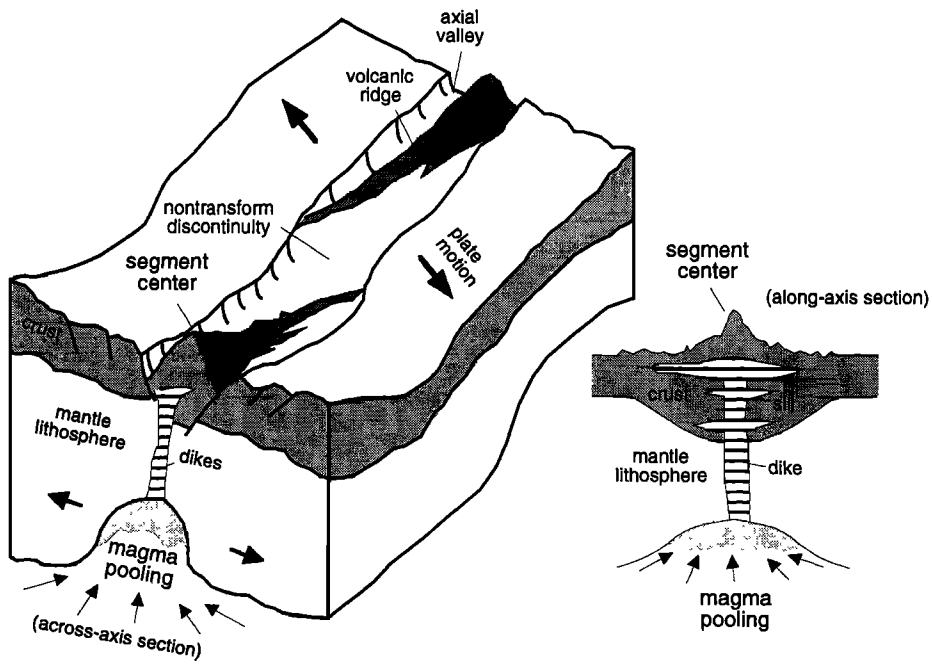

Figure 16. Interpretative block diagram showing two SWIR segments in the region east of the Melville transform. The axial valley is oblique to the spreading direction and is filled by volcanic ridges that trend perpendicular to the spreading direction and are highest at segments centers. These volcanic ridges are fed by dikes rooting in magma-rich regions at the base of the axial lithosphere. Across and along-axis sections show that magma pools preferentially beneath segments centers, where the lithosphere is thinner. Crustal thickening at segments centers occurs through both volcanic construction and the formation of sills in the lower crust. The along-axis section is derived from Figure 11.

and dikes would be more likely to make it to the near surface. The transition in the style of segmentation along the SWIR occurs near the Melville transform (Figure 4), with two segments from the Atlantis II to Melville region (17 and 19) showing intermediate bathymetry and gravity characteristics. The ridge between Atlantis II and Melville may therefore receive just about the critical melt supply, for the SWIR spreading rate. Calculated melt thickness values listed in Table 2 suggest that this critical melt supply may be of the order of 3.4 km. It is worth emphasizing that this low melt supply is not a result of slow spreading rates, as spreading rate does not vary in our study area, but of the low temperature of the subaxial mantle beneath the eastern regions of the SWIR.

5.2. Consequences for the Thermal Regime at the Ridge Axis

Ever since the early models by *Parker and Oldenburg* [1973] and *Sleep* [1975], heat advection due to magma emplacement in the oceanic crust has been modeled as the result of repeated magma intrusion in a thin dike-like region exactly at the ridge axis, so that material not exactly at the axis moves away at plate velocity. The height of this dike-like region is equal to crustal thickness in most models [e.g., *Sleep*, 1975; *Morton and Sleep*, 1985; *Phipps Morgan et al.*, 1987; *Lin and Parmentier*, 1989; *Chen and Morgan*, 1990; *Neumann and Forsyth*, 1993]. Heat advection occurs both because of the specific heat of the magma and because it releases latent heat upon crystallization [*Sleep*, 1975]. *Morton and Sleep* [1985] modeled hydrothermal cooling with heat sinks distributed near the axis in the domain thought to be affected by hydrothermalism. *Phipps Morgan et al.* [1987] then proposed to treat hydrothermal heat transport as an enhanced thermal conductivity within the temperature and depth range where hydrothermal activity is thought to occur. Thermal models of the axial lithosphere have since then consistently adopted this approach, with enhancement factors generally ranging between 6 and 10, cutoff temperatures for hydrothermal circulation of 400° to 600°C, and a cutoff depth of 6 km.

Although this modeling approach is well adapted to the intrusive component of the oceanic crust, it overemphasizes the heat contributed by the extrusive component, because lava flows rapidly lose their heat to the cold seawater [*Sleep*, 1991]. This will have little effect on ridges where extrusives are thin relative to the gabbroic and doleritic intrusive component of the crust. It should, however, have a significant effect in ridge portions where the crust includes large volcanic constructions. A large proportion of the heat advected to the center of high relief segments in the east of Melville region may thus be lost to seawater, either because it is carried by extruded lavas, or because it is carried by magma that crystallizes as shallow intrusives in volcanic edifices made of cool and highly permeable basalt flows. The thermal regime in the crust and upper mantle of these high relief segments is therefore likely to be colder, for a given magma budget, than predicted by conventional thermal models.

6. Conclusions

The principal conclusions of this paper are the following.

1. A significant part of the axial relief in segments from the east of Melville region is due to volcanic constructions that load the axial lithosphere from above. By contrast, the isostatic component of the axial relief in segments west of the Melville fracture zone would be primarily due to partial compensation of negative loads (thicker lower crust and/or lighter upper mantle) acting within the plate, or at the bottom of the plate. The length, relief, and gravity signature of these segments are less variable than in the east of Melville region and are similar to those measured along the faster spreading Mid-Atlantic Ridge. The length, relief, and gravity signature of the east of Melville ridge segments are highly variable. The change in crustal thickness between the center and the ends of the highest relief segments is estimated (from MBA variations) to be of the order of 3.5 km, the estimated height of associated volcanic constructions being of the order of 1500 m. In these high relief segments, the uppermost, mostly extrusive, part of the crust would therefore contribute about two fifths of segment scale crustal thickness variations. Hydrothermal heat loss should be higher in these permeable extrusive basalts than in deeper crustal levels. The thermal regime of high relief SWIR segments is therefore likely to be colder, for a given magma budget, than in segments that have a lesser proportion of extrusive lavas in the crust.

2. In order to form large volcanic constructions on the seafloor of a slow spreading ridge, magma must be rapidly transported upward from the top of the melting region and through the thick axial lithosphere. This transport is most likely to occur in dikes that root in a melt-rich region near the base of the axial lithosphere. Stress conditions in the axial lithosphere should determine whether these dikes stop their upward propagation and feed sills within the upper mantle and lower crust or propagate all the way up to build volcanoes on the seafloor. These stress conditions are likely to be affected by the frequency of dike injections, itself a function of melt supply, at a given spreading rate. The transition in the style of segmentation along the SWIR occurs near the Melville transform, with two segments from the Atlantis II to Melville region showing intermediate bathymetry and gravity characteristics. This region of the SWIR may thus receive just about the critical melt supply for the SWIR spreading rate.

3. Differences in regional axial depths within the study area are consistent with the ridge east of Melville fracture zone having a lower melt supply and being underlain by cold mantle. Mantle temperatures at solidus calculated for this eastern region are substantially colder than the 1342°C "normal" mantle temperature of our melting model (corresponding to the production of a melt thickness of 6 km by adiabatic melting). This is consistent with the existence of a broad positive anomaly of *S* waves velocities [*Debayle and Lévêque*, 1997] in the mantle of this region, and with geochemical data presently available on dredged basalts [*Robinson et al.*, 1996; *C. Mével et al.*, unpublished results, 1997]. The melt thickness calculated in our model for this cold region of the ridge is about 2.7 km. The presence of a significant proportion of serpentinized peridotites in the crust of this region would translate into even colder regional mantle temperatures and smaller regional melt thicknesses. Conversely, a deeper compensation depth for isostatic balance calculations in this cold part of the ridge would lead to slightly higher computed regional mantle temperatures and melt thicknesses. Calculated differences in mantle temperature (at a depth of 90 km) and in melt thickness (for a crust made only of magmatic rocks and a compensation depth of 200 km) between this cold and deep eastern region, and the shallower region west of the Gallieni FZ, are of the order of 80°C and 4

km, respectively. Ridge segments to the east of Melville receive less melt on average, yet along-axis MBA variations have a similar range of amplitudes all over our study area. This suggests that a larger proportion of the magma that is extracted from the mantle is focused toward the center of segments in cold than in hotter regions of the SWIR.

Appendix A. Intrasegment Crustal Thickness Variations

MBA that results from sinusoidal topography at the crust mantle interface (sinusoidal variations of crustal thickness ΔC) can be expressed as:

$$\Delta\text{MBA} = 2\pi\,(\rho_m - \rho_c)\,G\,\exp^{(-2\pi H/\lambda)}\,\Delta C$$

where λ is the wavelength of crustal thickness variations, G is the gravitational constant, ρ_m is the mantle density (3300 kg/m^3), ρ_c is the crust density (2700 kg/m^3), and H is the mean Moho depth (below sea level). H is set here as 9 km, as in MBA calculations [*Rommevaux-Jestin et al.*, 1997].

Appendix B. Regional Variations in Axial Depth, Melt Thickness, and Mantle Temperature

Potential temperatures are calculated with an adiabatic gradient of 0.3°/km, and a conductive profile expressed as

$$T_{\text{cond}}(z) = C_1\,\exp^{(-u/k)\,z} + C_2,$$

where u is the mantle upwelling velocity in m/s (here the half spreading rate; see Figure 12), k is the thermal diffusivity of mantle rocks (8.04 10^{-7} m^2/s), z is the depth below seafloor in meters, and C_1 and C_2 are constants fitting the boundary conditions. We make the approximation that at a depth of 90 10^3 m (z_0), the effect of conductive cooling is negligable: $T(z_0) = C_2$. The general equation for potential temperatures in the mantle is therefore

$$T_{\text{pot}}(z) = T(z0) + C_1\,\exp^{(-u/k)\,z} - 0.3\,(z_0 - z).$$

In setting A, C_1 is such that $T_{\text{pot}}(z = 5\ 10^3\ \text{m}) = 500°\text{C}$; in setting B, C_1 is such that $T_{\text{pot}}(z = 10^4\ \text{m}) = 500°\text{C}$. The melting rate ($F$) is expressed [*Langmuir et al.*, 1992] as

$$F(z) = (T_{\text{pot}}(z) - T_{\text{sol}}(z)) / ((Hf/Cp) + (dT/dF)),$$

with $T_{\text{sol}}(z) = 1100 + 3.9\ 10^{-3}\ z$, Hf (latent heat of melting) = 753 J/g.°, Cp (heat capacity) = 1.25 J/g, and $dT/dF = 3.5°/\%$.

Crustal thickness, mean F, and the mean depth of melting are calculated as explained in the thick lithosphere setting of Figure 50 of *Langmuir et al.* [1992].

A test of this 1-D analytical melting model against the 2-D numerical approach of *Bown and White* [1994] is shown in Figure B1. For this test we have compared melting rates calculated with the two methods for a mantle temperature at solidus of 1300°C, using the same boundary conditions ($T_{\text{pot}}(z = 0) = 0°\text{C}$), and a Hf value of only 418 J/g°. For a half spreading rate of 10 mm/yr (i.e., faster than at the SWIR), the 1-D model yields slightly higher values for the maximum melting rate (F_{max}) than Bown and White's model. By contrast, for a half spreading rate of 5 mm/yr (i.e., slower than at the SWIR), the 1-D model yields slightly lower F_{max} values than Bown and White's model. This is because in this model the wedge angle of the melting domain, and therefore the mantle

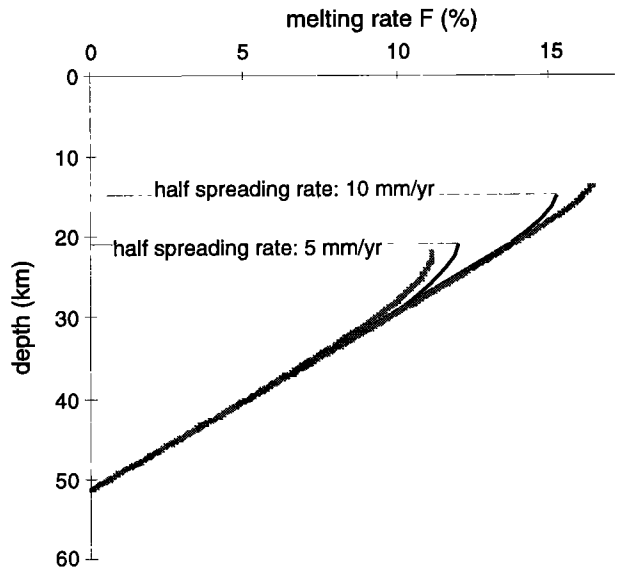

Figure B1. A comparison of melting rate versus depth curves obtained with our 1-D thermal and melting model (solid curves) and with the 2-D model of *Bown and White* [1994] (grey curves) for two values of the half spreading rate (5 and 10 mm/yr) and for a mantle temperature at solidus of 1300°C. Boundary conditions and melting parameters are the same as given by *Bown and White* [1994].

upwelling velocities (Figure 12), increase with decreasing spreading rate. At half spreading rates between these two values, and therefore at the SWIR half spreading rate (8 mm/yr), the agreement between the two models is good.

Relative variations in regional axial depths are calculated for the isostatically balanced columns represented in Figure 13 with

$$\Delta H = (\rho_m - \rho_c)/(\rho_m - \rho_w)\,\Delta C + \alpha/(\rho_m - \rho_w)\,Z\,\Delta T_m \rho_m,$$

where α is the coefficient of thermal expansion in mantle rocks: 3 10^{-5} K^{-1}, Z is the depth of compensation: 200 km and ΔT_m is the average temperature of the mantle between Z and the base of the crust. To calculate ΔT_m, we used the thermal structure of Figure 12 up to the top of the melting region (adiabatic gradient below the solidus, then melting path between the solidus and the top of the melting column) and an arbitrary average temperature of 900°C for the mantle between the top of the melting region and the base of the crust.

Estimates of mean F from the sodium content of SWIR basalts are made as explained by *Klein and Langmuir* [1987], using the following equation:

$$\text{Na}_{8.0} = (\text{Na}_0 / \text{mean } F)\,(1 - (1\text{-mean } F)^{1/D}),$$

where $\text{Na}_{8.0}$ is the sodium content of basalts corrected for fractionation, Na_0 is the sodium content of the mantle source (here 0.29%), and D is the partition coefficient of sodium between melt and mantle (here 0.035).

Acknowledgements. We thank Jian Lin, Uri Ten Brink, an anonymous reviewer and Mark Muller for their help in revising this paper. We also thank P. Patriat for inviting us on the Gallieni cruise of R.V. *L'Atalante*. This study was supported by CNRS-INSU, "Géosciences Marines" Program.

References

Blackman, D.K., and D.W. Forsyth, Isostatic compensation of tectonic features of the Mid-Atlantic Ridge 25-27°30'S, *J. Geophys. Res*, *96*, 11,741-11,758, 1991.

Bown, J.W., and R.S. White, Variation with spreading rate of oceanic crustal thickness and geochemistry, *Earth Planet. Sci. Lett.*, *121*, 435-449, 1994.

Cannat, M., Emplacement of mantle rocks in the seafloor at mid-ocean ridges, *J Geophys. Res.*, *98*, 4163-4172, 1993.

Chen, Y., and W.J. Morgan, A nonlinear rheology model for mid-ocean ridge axis topography, *J. Geophys. Res.*, *95*, 17,583-17,604, 1990.

Debayle, E., and J J Lévêque, Upper mantle heterogeneities in the Indian Ocean from waveform inversions, *Geophys. Res. Lett*, *24*, 245-248, 1997.

DeMets, C., R.G Gordon, D.F. Argus, and C. Stein, Current plate motion, *Geophys. J. Int.*, *101*, 425-478, 1990.

Detrick, R.S., H.D Needham, and V. Renard, Gravity anomalies and crustal thickness variations along the Mid-Atlantic Ridge between 33°N and 40°N, *J. Geophys. Res.*, *100*, 3767-3787, 1995.

Dick, H.J.B., Abyssal peridotites, very slow spreading ridges and ocean ridge magmatism, in *Magmatism in the Ocean Basins*, edited by A.D. Saunders and M.J. Norris, *Geol Soc. Spec. Publ.*, *42*, 71-105, 1989

Dick, H.J.B, H. Schouten, P.S. Meyer, D.G. Gallo, H. Bergh, R Tyce, P. Patriat, K.T.M. Johnson, J. Snow, and A. Fisher, Tectonic evolution of the Atlantis II Fracture Zone, *Proc. Ocean Drill Program Sci Results*, *118*, 359-398, 1991.

Fox, P.J., N.R. Grindlay, K.C. Macdonald, S.M. Carbotte, D.W. Forsyth, and B.Y. Kuo, The Mid-Atlantic Ridge (31°-34°S). Temporal and spatial variations of accretionary processes, *Mar. Geophys. Res.*, 13, 1-20, 1991.

Gente, P., R. Pockalny, C. Durand, C. Deplus, M. Maia, G. Ceuleneer, C. Mével, M. Cannat, and C. Laverne, Characteristics and evolution of the segmentation of the Mid-Atlantic Ridge between 20°N and 24°N during the last 10 million years, *Earth Planet Sci. Lett*, *129*, 55-71, 1995.

Grindlay, N R., P.J Fox, and K.C. Macdonald, Second Order Ridge Axis Discontinuities in the South Atlantic: Morphology, Structure and Evolution, *Mar. Geophys. Res*, *13*, 21-49, 1991.

Grindlay, N.R., P.J. Fox, and P.R. Vogt, Morphology and tectonics of the Mid-Atlantic Ridge (25°S-27°30'S) from SeaBeam and magnetic data, *J. Geophys. Res.*, *13*, 21-49, 1992.

Grindlay, N.R., J. Madsen, C. Rommevaux, and J. Sclater, A different pattern of ridge segmentation and mantle Bouguer gravity anomalies along the ultra-slow spreading Southwest Indian Ridge (15°30'E to 25°E), *Earth Planet Sci. Lett.*, *161*, 243-253, 1998.

Gudmundson, A., Emplacement of dikes, sills and crustal magma chambers at divergent plate boundaries, *Tectonophysics*, *176*, 257-275, 1990.

Huang, P.Y., and S.C. Solomon, Centroid depths of mid-ocean ridge earthquakes: Dependence on spreading rates, *J Geophys. Res.*, *93*, 13,445-13,477, 1988.

Ito, G., and J. Lin, Oceanic spreading center-hot spot interactions: Constraints from along-isochron bathymetric and gravity anomalies, *Geology*, *23*, 657-660, 1995.

Kirby, S.H., Rheology of the lithosphere, *Rev. Geophys.*, *21*, 1458-1483, 1983.

Klein, E.M., and C H. Langmuir, Global correlations of ocean ridge basalt chemistry with axial depth and crustal thickness, *J. Geophys. Res*, *92*, 8089-8115, 1987.

Kong, L.S., S.C. Solomon, and G.M. Purdy, Microearthquake characteristics of a mid-ocean ridge along-axis high, *J Geophys. Res.*, *97*, 1659-1685, 1992.

Kuo, B.Y., and D.W. Forsyth, Gravity anomalies of the ridge-transform system in the South Atlantic between 31° and 34.5°S: Upwelling centers and variations in crustal thickness, *Mar. Geophys. Res*, *10*, 205-232, 1988.

Langmuir, C.H., E.M. Klein, and T. Plank, Petrological systematics of mid-ocean ridge basalts: Constraints on melt generation beneath ocean ridges, in *Mantle Flow and Melt Generation at Mid-Ocean Ridges*, *Geophys. Monogr. Ser.*, vol. 71, edited by J. Phipps Morgan et al., pp. 183-280, AGU, Washington, D.C., 1992.

Lin, J., and E.M. Parmentier, Mechanisms of lithospheric extension at mid-ocean ridges, *Geophys. J.*, *96*, 1-22, 1989.

Lin, J., G.M. Purdy, H. Schouten, J.C. Sempéré, and C Zervas, Evidence from gravity data for focused magmatic accretion along the Mid-Atlantic Ridge, *Nature*, *344*, 627-632, 1990.

Lin, J., and J. Phipps Morgan, The spreading rate dependence of three-dimensional mid-ocean ridge gravity structure, *Geophys. Res. Lett*, *19*, 13-16, 1992

Lister, J.R, and R C. Kerr, Fluid-mechanical models of crack propagation and their application to magma transport in dykes, *J Geophys. Res.*, *96*, 10,049-10,077, 1991.

Macdonald, K.C., Mid-ocean ridges: fine scale tectonics, volcanic and hydrothermal processes within the plate boundary zone, *Annu. Rev. Earth Planet. Sci.*, *10*, 155-190, 1982

Macdonald, K.C., P.J. Fox, L.J Perram, M F. Eisen, R M Haymon, S.P. Miller, S.M. Carbotte, M.H. Cormier, and A.N. Shor, A new view of the Mid-Ocean Ridge from the behavior of ridge-axis discontinuities, *Nature*, *335*, 217-225, 1988.

Magde, S.G., D.W Sparks, and R.D. Detrick, The relation between buoyant mantle flow, melt migration, and gravity bull's eyes at the Mid-Atlantic Ridge between 33°N and 35°N, *Earth Planet. Sci Lett.*, *148*, 59-67, 1997.

Mendel, V., and D. Sauter., Seamount volcanism at the super slow spreading Southwest Indian Ridge between 57°E and 70°E, *Geology*, *25*, 99-102, 1997.

Mendel, V, D. Sauter, L.M. Parson, and J.R. Vanney, Segmentation and morphotectonic variations along an ultra-slow spreading center: The South-West Indian Ridge (57°E-70°E), *Mar Geophys. Res*, *19*, 505-533, 1997

Mével, C., et al, Sampling the Southwest Indian Ridge: First results of the EDUL cruise (R/V *Marion Dufresne II*, August 1997), *InterRidge News*, *6-2*, 25-26, 1997

Minshull, T.A., M.R. Muller, C.J Robinson, R S. White, and M J. Bickle, Is the oceanic Moho a serpentinization front?, in *Modern Ocean Floor Processes and the Geological Record*, edited by R.A. Mills, and K. Harrison, *Geol. Soc. Spec. Publ*, *148*, 71-80, 1998.

Morton, J.L., and N.H. Sleep, A mid-ocean ridge thermal model. Constraints on the volume of axial hydrothermal heat flux, *J. Geophys Res*, *90*, 11,345-11,353, 1985

Muller, M R, C.J. Robinson, T.A Minshull, R.S. White, and M.J. Bickle, Thin crust beneath ocean drilling program borehole 735B at the Southwest Indian Ridge?, *Earth Planet Sci. Lett*, *148*, 93-107, 1997.

Muller, M.R., T A. Minshull, and R S. White, Crustal structure and segmentation on the SWIR at 66°E (abstract), European Geophysical Society Symposia, *Ann. Geophys.*, *16*, 294, 1998.

Munschy, M., and R Schlich, Etude géophysique des dorsales de l'Océan Indien dans la région du Point Triple de Rodriguez, *Oceanologica Acta*, *10*, 119-128, 1990.

Neumann, G.A, and D W. Forsyth, The paradox of the axial profile: Isostatic compensation along the axis of the Mid-Atlantic Ridge?, *J Geophys Res.*, *98*, 17,891-17,910, 1993

Parker, R.L., and D.W. Oldenburg, Thermal model of ocean ridges, *Nature*, *242*, 137-139, 1973

Patriat, P., and J Segoufin, Reconstruction of the central Indian Ocean, *Tectonophysics*, *155*, 211-234, 1988.

Patriat, P., and the Gallieni and Capsing cruise scientific party, Segmentation of the Southwest Indian Ridge from 49°E to the triple junction [70°E]. What is the mark of a very slow spreading rate? (abstract), *Eos, Trans AGU*, *77* (46), Fall Meet. Suppl., 689, 1996.

Patriat, P., D Sauter, M. Munschy, and L. Parson, A survey of the Southwest Indian Ridge axis between Atlantis II FZ and the Indian Ocean Triple Junction: Regional setting and large-scale segmentation, *Mar. Geophys. Res.*, *19*, 457-480, 1997.

Phipps Morgan, J., and Y.J Chen, The genesis of oceanic crust: Magma injection, hydrothermal circulation, and crustal flow, *J. Geophys. Res*, *98*, 6283-6297, 1993.

Phipps Morgan, J., E.M. Parmentier, and J Lin, Mechanisms for the origin of mid-ocean ridge axial topography: Implications for the thermal and mechanical structure of accreting plate boundaries, *J Geophys. Res*, *92*, 12,823-12,836, 1987

Prince, R.A, and D.W. Forsyth, Horizontal extent of anomalously thin crust near the Vema Fracture Zone from 3-dimensional analysis of gravity anomalies, *J. Geophys. Res.*, *93*, 8051-8063, 1988.

Purdy, G.M., and R.S. Detrick, Crustal structure of the Mid-Atlantic Ridge at 23°N from seismic refraction studies, *J Geophys Res.*, *91*, 3739-3762, 1986.

Reid, I., and H.R. Jackson, Oceanic spreading rate and crustal thickness, *Mar Geophys. Res.*, *5*, 165-172, 1981.

Robinson, C.J., R.S. White, M.J. Bickle, and T.A. Minshull, Restricted melting under the very slow spreading Southwest Indian Ridge, in *Tectonic, Magmatic, Hydrothermal and Biological Segmentation of*

Mid-Ocean Ridges, edited by C.J. MacLeod et al., *Geol. Soc. Spec. Publ., 118*, 131-141, 1996.

Rommevaux, C., C. Deplus, P. Patriat, and J C. Sempéré, Three-dimensional gravity study of the Mid-Atlantic Ridge: Evolution of the segmentation between 28° and 29°N during the last 10 Myr, *J. Geophys. Res., 99*, 3015-3030, 1994.

Rommevaux-Jestin, C., C. Deplus, and P. Patriat, Mantle Bouguer anomaly along an ultra-slow spreading ridge: Implications for accretionary processes and comparison with results from Central Mid-Atlantic Ridge, *Mar. Geophys Res., 19*, 481-503, 1997.

Rubin, A.M., A comparison of rift-zone tectonics in Iceland and Hawaii, *Bull. Volcanol., 52*, 302-319, 1990.

Rubin A.M., and D D. Pollard, Origins of blade-like dikes in volcanic rift zones, *U.S. Geol. Surv. Prof. Pap., 1350*, 1449-1470, 1987.

Sandwell, D.T., and W.H.F. Smith, Marine gravity anomaly from Geosat and ERS-1 satellite altimetry, *J. Geophys. Res , 112*, 11,039-11,054, 1997.

Sauter, D., V. Mendel, C. Rommevaux-Jestin, P. Patriat, andM. Munschy, Propagation of the South-West Indian Ridge at the Rodriguez Triple Junction, *Mar. Geophys. Res., 19*, 553-567, 1997.

Sempéré, J.C., J. Lin, H.S. Brown, H. Schouten, and G.M. Purdy, Segmentation and morphotectonic variations along a slow spreading center: The Mid-Atlantic Ridge (24°00'N-30°40'N), *Mar. Geophys. Res., 15*, 153-200, 1993.

Shaw, W.T., and J. Lin, Models of oceanic ridge lithospheric deformation. Dependence on crustal thickness, spreading rate, and segmentation, *J. Geophys. Res., 101*, 17,977-17,993, 1996.

Sinton, J.M., and R.S Detrick, Mid-ocean ridge magma chambers, *J. Geophys. Res., 97*, 197-216, 1992.

Sleep, N.H., Formation of ocean crust: Some thermal constraints, *J. Geophys. Res., 80*, 4037-4042, 1975.

Sleep, N.H., Tapping of melt by veins and dikes, *J. Geophys. Res., 93*, 10,255-10,272, 1988.

Sleep, N.H., Hydrothermal circulation, anhydrite precipitation, and thermal structure at ridge axes, *J. Geophys. Res.*, 96, 2375-2387, 1991.

Sleep, N.H., and G.A. Barth, The nature of the oceanic lower crust and shallow mantle emplaced at slow spreading rates, *Tectonophysics, 279*, 181-192, 1997.

Spiegelman, M., and D. McKenzi.e, Simple 2-D models for melt extraction at mid-ocean ridges and island arcs, *Earth Planet. Sci. Lett., 83*, 137-152, 1987.

Sparks, D.W., and E.M. Parmentier, Melt extraction from the mantle beneath spreading centers, *Earth Planet. Sci. Lett., 105*, 368-377, 1991.

Tapponnier, P., and J Francheteau, Necking of the lithosphere and the mechanics of slowly accreting plate boundaries, *J. Geophys. Res., 83*, 3955-3970, 1978.

Thibaud, R., P. Gente, and M. Maia, A systematic analysis of the Mid-Atlantic Ridge morphology and gravity between 15°N and 40°N: Constraints on the thermal structure, *J. Geophys. Res., 103*, 24,223-24,243, 1998.

Tolstoy, M., A.J. Harding, and J.A. Orcutt, Crustal structure on the Mid-Atlantic Ridge: Bull's-eye gravity anomalies and focused accretion, *Science, 262*, 726-729, 1993.

Toomey, D.R., S.C Solomon, G.M. Purdy, and M.H. Murray, Microearthquakes beneath the median valley of the Mid-Atlantic Ridge near 23°N: Tomography and tectonics, *J. Geophys. Res., 93*, 9093-9112, 1988.

Wang, X., and J.R. Cochran, Along-axis gravity gradients at mid-ocean ridges. Implications for mantle flow and axial morphology, *Geology, 23*, 29-32, 1995.

White, R.S., D. McKenzi.e , and R.K. O'Nions, Oceanic crustal thickness from seismic measurements and rare earth element inversions, *J. Geophys. Res., 97*, 19,683-19,715, 1992.

Whitehead, J.A., H.J.B. Dick, and H. Schouten, A mechanism for magmatic accretion under spreading centers, *Nature, 312*, 146-148, 1984.

Wolfe, C.J., G.M. Purdy, D.R. Toomey, and S.C. Solomon, Microearthquake characteristics and crustal velocity structure at 29°N on the Mid-Atlantic Ridge. The architecture of a slow spreading ridge, *J. Geophys. Res., 100*, 24,449-24,472, 1995.

M. Cannat and C. Rommevaux-Jestin, CNRS-UPRESA 7058, Laboratoire de Pétrologie, Université Pierre et Marie Curie, 4 pl. Jussieu, 75252 Paris cedex 05, France. (cannat@ccr.jussieu.fr)

C. Deplus, CNRS-UMR 7577, Laboratoire de Gravimétrie, Institut de Physique du Globe, 4 pl. Jussieu, 75252 Paris cedex 05, France.

V. Mendel, Challenger Division for Seafloor Processes, Southampton Oceanography Center, Empress Dock, Southampton SO143ZH, England, UK.

D Sauter, CNRS-UMR JO533, Institut de Physique du Globe, Université de Strasbourg, 5 rue R. Descartes, 67084 Strasbourg, France.

(Received July 8, 1998; Revised April 19, 1999;
accepted June 2, 1999.)